



## 저작자표시-비영리-변경금지 2.0 대한민국

이용자는 아래의 조건을 따르는 경우에 한하여 자유롭게

- 이 저작물을 복제, 배포, 전송, 전시, 공연 및 방송할 수 있습니다.

다음과 같은 조건을 따라야 합니다:



저작자표시. 귀하는 원저작자를 표시하여야 합니다.



비영리. 귀하는 이 저작물을 영리 목적으로 이용할 수 없습니다.



변경금지. 귀하는 이 저작물을 개작, 변형 또는 가공할 수 없습니다.

- 귀하는, 이 저작물의 재이용이나 배포의 경우, 이 저작물에 적용된 이용허락조건을 명확하게 나타내어야 합니다.
- 저작권자로부터 별도의 허가를 받으면 이러한 조건들은 적용되지 않습니다.

저작권법에 따른 이용자의 권리는 위의 내용에 의하여 영향을 받지 않습니다.

이것은 [이용허락규약\(Legal Code\)](#)을 이해하기 쉽게 요약한 것입니다.

[Disclaimer](#)

공학박사학위논문

**A study on poly(lactic acid) and natural rubber  
blends compatibilized by organoclays**

유기 점토입자로 상용화된 폴리락틱산/천연고무  
블렌드에 관한 연구

2016 년 8 월

서울대학교 대학원

화학생물공학부

옥 현 근

## **Abstract**

# **A study on poly(lactic acid) and natural rubber blends compatibilized by organoclays**

Hyun Geun Ock

School of Chemical and Biological Engineering

Seoul National University

In this thesis, the effect of organoclay as a compatibilizer in immiscible poly(lactic acid) (PLA) and natural rubber (NR) blends was studied. Structural development of PLA90/NR10 blend was examined depending on the clay content (0.5~10wt%). The drop size of the dispersed NR phase initially decreased and then remained constant as the clay content increased. Below the critical concentration (3wt%), the clay was selectively localized mostly at the interface between the matrix phase (PLA) and the dispersed phase (NR), whereas the clay particles were additionally observed in the matrix phase above 3wt%. XRD analysis revealed that the gallery structure of the clay was highly dependent on the concentration and selective location of the clays. The development of the structure and the physical properties of the blend were also investigated according to the clay contents by measuring the linear viscoelasticity and surface tension. The degree of clay exfoliation was analyzed quantitatively in terms of the modulus ratio of PLA/NR/clay and PLA/clay. The elongational behavior and

mechanical properties of the blends were strongly dependent on the location of the clays. The clay worked as an efficient compatibilizer below the critical content, while it worked as a reinforcing filler above the threshold, making the matrix more rigid.

Next, the compatibilizing effect of organoclay in immiscible poly(lactic acid) (PLA) and natural rubber (NR) blends was investigated through small amplitude oscillatory shear (SAOS) and large amplitude oscillatory shear (LAOS) tests by varying clay concentrations, mixing conditions and types of clay. A quantified nonlinear parameter ( $I_{3/1}$ ) from FT-rheology and complex moduli ( $|G^*|$ ) were used to analyze the structural development of the PLA/NR blends in response to added clays. The nonlinear-linear viscoelastic ratio (NLR) was also introduced to describe morphological changes in the blends. Observation of the TEM images revealed that the drop size of natural rubber decreased as the clay content increased from 0.5 to 3 wt%. However, the NR size did not change above 3wt% of the clay. The NLR value increased up to 3wt%, then reached a plateau. The drop size reduction due to increased mixing rates was reflected in the NLR value. In addition, the compatibilization efficiency of various types of clay was in accordance with the NLR value. A reciprocal relationship was observed between the NLR and inverse of the drop size, with respect to the clay concentration, mixing condition, or types of clay. The NLR value could be used to estimate the compatibilizing effect of organoclay in immiscible polymer blends (PLA/NR), even without direct morphological observation.

**Keywords:** Poly(lactic acid), natural rubber, organoclay, polymer blend, compatibilization, extensional viscosity, FT-rheology, Q parameter, NLR

**Student Number:** 2013-30987

# Contents

Abstract.....	i
List of Contents.....	iv
List of Figures .....	vi
List of Tables .....	xi
<b>Chapter 1. Introduction.....</b>	<b>1</b>
1.1. General introduction.....	2
1.2. Outline of the thesis .....	5
<b>Chapter 2. Background .....</b>	<b>7</b>
2.1. Poly(lactic acid) and natural rubber blends.....	8
2.2. Effect of organoclay as a compatibilizer.....	12
2.3. Characterization of compatibilizing effect by FT-rheology .....	17
2.4. Objectives of the thesis .....	23
<b>Chapter 3. Experimental methods .....</b>	<b>24</b>
3.1. Sample preparation.....	25
3.2. Measurement of rheological property.....	29
3.3. Characterization of structure and properties of blends .....	30
<b>Chapter 4. Results and discussion.....</b>	<b>31</b>

4.1. Microstructure of PLA/NR/clay .....	32
4.1.1. Morphological development .....	32
4.1.2. Selective localization and dispersion quality of clay .....	35
4.2. Linear rheological analysis.....	39
4.2.1. Dynamic properties .....	39
4.2.1.1. Interfacial tension.....	44
4.2.1.2. Capillary number estimation.....	48
4.2.1.3. Effect of clay exfoliation .....	53
4.3. Elongational rheology.....	57
4.3.1. Extensional viscosity.....	57
4.3.2. Mechanical properties.....	61
4.4. Nonlinear rheological characterization.....	64
4.4.1. Concentration of clay .....	64
4.4.2. Mixing condition.....	82
4.4.3. Types of clay.....	87
4.4.1. Relation between NLR and drop diameter .....	96
<b>Chapter 5. Conclusion.....</b>	<b>98</b>
<b>References.....</b>	<b>101</b>
<b>국문 초록.....</b>	<b>114</b>

## List of Figures

<b>Figure 2.1.1.</b> Reaction schemes to produce PLA .....	10
<b>Figure 2.1.2.</b> Schematic representation for structure, thermal properties, and resources of PLA and natural rubber, respectively.....	11
<b>Figure 2.2.1.</b> Confocal microscopy images of PLA85/NR15, PLA90/NR10, and PLA85/NR15, respectively .....	14
<b>Figure 2.2.2.</b> TEM pictures of 10/90 (w/w) PBT/PE (a) and 80/20 (w/w) (b) with 5 phr organoclay.....	15
<b>Figure 2.2.3.</b> Samples stretched at different elongations (a) PLA, (b) PLA/NR, (c) PLA/NR/C15A 1wt%, (d) PLA/NR/C15A 3wt%.....	16
<b>Figure 2.3.1.</b> (a) Nonlinear stress curve, (b) FT-spectrum gained from FT-rheological analysis, respectively .....	20
<b>Figure 2.3.2.</b> NLR of PCL/MWNT, PCL/OMMT, PCL/PCC composites, and PVA/borax solution as function of concentration. The lines are added to guide eye.....	21
<b>Figure 2.3.3.</b> Comparison of NLR values of PP/PS/C20A and PP/PS/silica blends as a function of weight fraction of particles, and TEM images of PP/PS/ 5wt% C20A, PP/PS/ 7wt% C20A, PP/PS/ 5wt% silica, and PP/PS/ 7wt% silica, respectively .....	22
<b>Figure 3.1.1.</b> Structures of functional groups of (a) Cloisite 10A (C10A), (b) Cloisite 20A (C20A), (c) and Cloisite 30B (C30B). T: Tallow (~65% C18; ~30%	



C16; ~5% C14), HT: Hydrogenated Tallow (~65% C18; ~30% C16; ~5% C14) .....	27
<b>Figure 4.1.1.</b> Transmission Electron Microscopy (TEM) images of (a) PLA/NR, (b) PLA/NR/C20A3, and (c) PLA/NR/C20A10.....	33
<b>Figure 4.1.2.</b> Number-averaged diameter ( $D_n$ ) of the PLA/NR blends as a function of clay content.....	34
<b>Figure 4.1.3.</b> TEM images of the PLA/NR blends with different clay concentrations (0.5~10wt%) .....	36
<b>Figure 4.1.4.</b> XRD patterns of pristine C20A, PLA/NR and PLA/NR/C20A with different clay contents (0.5~10 wt%) .....	38
<b>Figure 4.2.1.</b> (a) Storage modulus ( $G'$ ), (b) loss modulus ( $G''$ ) and (c) complex viscosity ( $\eta^*$ ) of PLA/NR and PLA/NR/C20A as a function of angular frequency measured at 190°C.....	41
<b>Figure 4.2.2.</b> Tan $\delta$ of the PLA/NR/clay at 0.1 rad/s depending on the concentration of the clay (0~10 wt%).....	42
<b>Figure 4.2.3.</b> Weighted relaxation spectrum of (a) neat PLA and NR, and (b) PLA/NR and PLA/NR/C20A2. Inset: the spectrum of PLA/NR/C20A1, PLA/NR/C20A2 and PLA/NR/C20A3 in the high relaxation time regime.....	46
<b>Figure 4.2.4.</b> Estimated nominal capillary number ( $Ca_n$ ).....	50
<b>Figure 4.2.5.</b> TEM images for (a) PLA/C20A3 and (b) PLA/NR/C20A3. Scale bar is 500nm for (a) and 50nm for (b) .....	55
<b>Figure 4.2.6.</b> $\Psi$ as a function of clay content .....	56

<b>Figure 4.3.1.</b> Transient extensional viscosity as a function of time for the neat PLA and PLA/NR/C20A measured at 160°C .....	59
<b>Figure 4.3.2.</b> Trouton ratio of the neat PLA and PLA/NR/C20A with different clay content (0.5~10 wt%) .....	60
<b>Figure 4.3.3.</b> Elongation at break and tensile strength of the PLA/NR blend and PLA/NR/C20A measured at room temperature.....	62
<b>Figure 4.3.4.</b> Interparticle distance of the PLA/NR/C20A as a function of clay concentration.....	63
<b>Figure 4.4.1.</b> Linear rheological properties of PLA/NR blends filled with various concentrations of C20A particles, 0, 0.5, 1, 2, 3, 5, and 10wt% measured at 190°C, (a) absolute magnitude of complex modulus ( $ G^* $ ) as functions of applied frequency (b) $ G^* $ at 0.1 rad/s and terminal slope as a function of clay concentration (solid lines represent fitted results (b)) (c) storage moduli ( $G'$ ) (d) loss moduli ( $G''$ ) at four representative angular frequencies (0.1, 1, 10, and 100 rad/s).....	66
<b>Figure 4.4.2.</b> TEM images of PLA/NR blends with different C20A concentrations (0.5~0 wt%) with different magnification (scale bar is 500 nm for (a, b, c), 200 nm for (d, e, f) and 1 $\mu$ m for (g, h, i, j, k, l).....	68
<b>Figure 4.4.3.</b> Drop size ( $D_n$ , $D_{vs}$ ) of the PLA/NR blends with different concentrations of C20A.....	69
<b>Figure 4.4.4.</b> Highly zoomed-in TEM images for the PLA/NR blends with varied clay contents (a) 1wt% (b) 3wt% (c) 5wt%.....	70

<b>Figure 4.4.5.</b> $ G^* $ of PLA/NR blends with different amounts of C20A (0–10 wt%) as a function of strain amplitude at 190°C .....	73
<b>Figure 4.4.6.</b> Normalized Lissajous pattern under fixed frequency (1 rad/s) and different strain amplitudes (0.1, 0.25, 0.5, 1, 2) of PLA/NR blends with the concentration of C20A. (a) Total stress vs. normalized strain, (b) total stress vs. normalized strain rate (c), (d) zoomed-in plot for $\dot{\gamma}/\dot{\gamma}_{\max}$ vs $\sigma/\sigma_{\max}$ and $\dot{\gamma}/\dot{\gamma}_{\max}$ vs $\sigma/\sigma_{\max}$ for blends with 10 wt% C20A, respectively .....	74
<b>Figure 4.4.7.</b> (a) Normalized third harmonic intensity ( $I_{3/1}$ ) from FT-rheology versus strain amplitude of the PLA/NR blends reinforced with various concentrations of C20A, (b) Nonlinearity Q of the blend with different contents of C20A with strain amplitude (symbol: experiments, line: fitting results) .....	76
<b>Figure 4.4.8.</b> (a) Normalized $Q_0$ , and normalized $ G^* $ (b) NLR value determined by Eq. 4.4.1 for PLA/NR/C20A blends .....	80
<b>Figure 4.4.9.</b> $G'$ , $G''$ moduli of PLA/NR blends (left: without clay, right: with clay) measured at 0.1 rad/s 190°C. Clay (C20A) is added with 3wt% .....	83
<b>Figure 4.4.10.</b> (a) SEM pictures of PLA/NR and (b), (c) TEM pictures of PLA/NR/C20A3 blends compounded at different mixing rpm (30, 50 and 100 rpm corresponding to approximated shear rate 14.1 23.6 and 47.1 $s^{-1}$ , respectively) .....	85

<b>Figure 4.4.11.</b> (a) Storage and loss moduli of PLA/NR/C10A3, PLA/NR/C20A3 and PLA/NR/C30B3 with angular frequencies ( $G'$ and $G''$ are plotted separately in (b) and (c), respectively).....	88
<b>Figure 4.4.12.</b> TEM images of PLA/NR blends filled with different types of clays (3wt%). (a), (b) C10A, (c), (d) C20A, (e), (f) C30B .....	91
<b>Figure 4.4.13.</b> (a) $I_{3/1}$ as a function of strain amplitude, (b) comparison between $[Q_0(\phi)/Q_0]$ and $[G^*(\phi)/G^*(0)]$ for each blends (PLA/NR, PLA/NR/C30B3, PLA/NR/C20A3 and PLA/NR/C10A3). All clay (C30B, C20A, C10A) is added 3wt% on PLA/NR blends .....	93
<b>Figure 4.4.14.</b> (a) NLR value and (b) inverse volume-to-surface averaged drop diameter ( $1/D_{vs}$ ) of PLA/NR blends with 3wt% of different types of clay (C10A, C20A, C30B) .....	94
<b>Figure 4.4.15.</b> $1/D_{vs}$ vs. NLR (solid line represents fitted results). (a) linear-linear plot and (b) linear-log plot .....	97

## List of Tables

<b>Table 3.1.1.</b> Information of polymers used in the study .....	28
<b>Table 4.2.1.</b> Complex viscosity at 0.1 rad/s and terminal slope of the PLA/NR blends with different contents of organoclay.....	43
<b>Table 4.2.2.</b> Interfacial tension between PLA and NR and the parameters used to calculate it .....	47
<b>Table 4.2.3.</b> Viscosity of the dispersed phase and the matrix phase and their ratio at a given shear rate ( $47.1 \text{ s}^{-1}$ ) depending on the clay content in the PLA / NR blends.....	51
<b>Table 4.2.4.</b> Assumptions made to calculate nominal capillary number .....	52
<b>Table 4.4.1.</b> $D_n$ , $D_{vs}$ and PI values of the PLA90/NR10 with various contents of C20A (0~10wt%).....	71
<b>Table 4.4.2.</b> Fitting parameter of PLA/NR/C20A with different clay contents (0~10wt%).....	77
<b>Table 4.4.3.</b> $Q_0/Q_0(0)$ , $G^*/G^*(0)$ and NLR value of PLA90/NR10 blends with different concentration of C20A (0~10 wt%).....	81
<b>Table 4.4.4.</b> $Q_0$ , $ G^* $ , NLR of PLA90/NR10/C20A3 blends with different mixing rpm (30, 50, 100) .....	86
<b>Table 4.4.5.</b> Surface tension ( $\gamma$ ) and wetting coefficient ( $\omega_a$ ) of each material calculated by Eq. 4.1.1.....	89

<b>Table 4.4.6.</b> List of $Q_0/Q_0(0)$ , $G^*/G^*(0)$ and NLR value of PLA90/NR10 blends with 3wt% of different types of clay (C10A, C20A, C30B) measured 1 rad/s at 190°C .....	95
--	----

# **Chapter 1.**

## **Introduction**

## **1.1. General introduction**

A physical mixture of two or more polymers is defined as polymer blend. Polymer blends have been used for several decades due to the recent demand for special engineering application. Desired physical properties for specific purposes can be easily achieved with appropriate choices of multiple polymeric materials rather than synthesis of a new polymer. Accordingly, polymer blends occupy very important portion in actual polymer industry, even in economic aspects.

In general, the morphology of dispersed phase is changed from nodule, fibril shape to co-continuous phase with different viscosity ratio and volume ratio between matrix phase and dispersed phase. The size of droplet of the dispersed phase vary depending on interfacial stress and hydrodynamic stress following drop breakup and coalescence [1]. The shape and size of droplet of the secondary polymer would play one of the most important roles in controlling final properties of the polymer blends. We have to control the morphology of the blends in order to get required performance of the blends. Behavior of materials in molten state under the applied shear rate in manufacturing steps could be interpreted by rheological analysis. The first objective of this thesis is rheological investigation on morphology of polymer blends and relevant physical properties.

Another method to improve physical properties of polymer is introducing small amount of nanoparticles in polymer matrices. This hybrid material system is called polymer nanocomposites. Especially, clay is one of the most widely used nanoparticles to fabricate polymer nanocomposites due to its large surface area and



high aspect ratio. The performance of polymers such as mechanical properties [2,3], heat resistance [4,5], flame retardancy [6,7], gas barrier properties [8,9], and biodegradability [10,11] could be enhanced with relatively small amount of clay content compared to conventional micron-sized fillers [12]. Taken polymer blend and polymer nanocomposites together, three component material system which could be classified into polymer blend nanocomposites is achieved. Researches on polymer blend nanocomposites have been robust, since introducing two polymers and one nanoparticle is easier way to achieve required performances than developing of a new synthetic techniques of polymer.

Most of two polymers are immiscible each other, so that their blend exhibits phase separated morphology, which results in decrease of various mechanical properties. Unique features of each polymer can be revealed only when two polymers are efficiently blended. Thus, the additional compatibilizer is required to make two polymers more compatible in order to get desired features of each polymer [13,14]. Adopting polymer blend nanocomposite system, we can expect not only compatibilization of two immiscible polymers, but also enhancement of physical properties due to functionality of nanoparticles. In this thesis, strategies for compatibilization of immiscible polymer blends was also studied by choosing an immiscible polymer blend model system.

Dealing with complex material system, it is essential to design optimum composition between each materials. For example, more amounts of secondary polymer added to base polymer would result in decrease of intrinsic properties of base polymer. Also, excess amount of nanoparticle might be insignificant or even affect

negatively on certain properties. Thus, it is very important to decide the optimum amount of components, at which each of them could play its intrinsic role appropriately. This thesis focused on establishing strategies to determine the optimum ratio between materials of the model polymer blend nanocomposite to get the best performance.

## **1.2. Outline of the thesis**

The thesis contains background, experimental methods, results and discussion, and conclusion chapters.

Chapter 2 covers the background of the study which is categorized into three parts. The first part describes basic characteristic features of poly(lactic acid) (PLA) and explains inevitable reasons for blending it with highly elastic natural rubber (NR) to achieve better performances for industrial applications. In Chapter 2.2, immiscibility between PLA and NR is depicted, underlying the necessity of the use of compatibilizer to make the two polymers compatible to each other. There are several strategies to increase compatibility between the two polymers. An effective aspect of introducing organoclay among many kinds of compatibilizer is described as well. Then, nonlinear rheological analysis techniques utilizing FT-rheology to characterize compatibilizing effect of organoclay in PLA/NR blends is introduced in Chapter 2.3. Finally, the objectives of the thesis is suggested in Chapter 2.4.

Chapter 3 describes experimental methods, including material information of PLA, NR, and organoclays and sample preparation procedures. Chapter 3.2 deals with detailed description on rheological measurement, those of not only dynamic and extensional rheology, but also nonlinear rheological approaches by FT-rheology. In order to confirm microstructural development of the PLA/NR blends due to added organoclay, electron microscopy, such as SEM and TEM, was introduced in Chapter 3.3. In addition, other characterization tools, such as mechanical property and X-ray diffraction, are also described.

Chapter 4 describes the results about structure and properties of the PLA/NR/clay system resulting from compatibilization. In Chapter 4.1, microstructural features of PLA and natural rubber blends attributed to the effect of organoclay as a compatibilizer are described. In Chapter 4.2, structural development of the PLA/NR/clay is demonstrated on the basis of rheological analysis followed by interfacial tension analysis and capillary number estimation. In addition, effect of clay exfoliation on the blends is investigated. In Chapter 4.3, extensional viscosity and mechanical properties of the PLA/NR blends due to the presence of organoclay are described. The last part covers nonlinear rheological characteristics of the blends. Linear ( $G^*$ ) and nonlinear ( $Q$ ) rheological properties as well as the ratio between the two quantities (NLR) are introduced to trace morphological change of the blends for three important variables such as concentration of clay, mixing condition, and types of clay.

Chapter 5 summarizes the results of PLA and NR blends compatibilized by organoclays and then the thesis is concluded.

# **Chapter 2.**

## **Background**

## **2.1. Poly(lactic acid) and natural rubber blends**

Recently, we have been faced environmental problems of non-degradable plastic materials. Use of biodegradable polymers can be a solution for this kind of issues, as they are sustainable resources. Poly(lactic acid) (PLA) is a thermoplastic bio-polymer made from starch or aliphatic biodegradable polyester such as lactic acid as shown in Figure 2.1.1 [15,16]. PLA possesses various advantageous physical properties of other commercial plastic materials while having low cost for disposal because it is biodegradable [17-19]. PLA has good performances in biodegradability, biocompatibility, thermal stability, and excellent processability. Because it can be decomposed by bacteria or microorganisms, PLA has gained much attention as an alternative to non-biodegradable plastics. However, it has restrictions for industrial applications due to its brittleness, long degradation time, and low melt strength. PLA should be plasticized to enable its use in many industrial applications due to its innate brittleness [16,20]. One possible approach to overcome these drawbacks is to use plasticizers [21,22]. However, this causes additional problems in melt compounding. The use of typical liquid type plasticizers results in many problems such as evaporation of the plasticizer owing to the high shear stress and heat energy in the melt mixing process. Another possible method of plasticizing is introduction of highly elastic toughening materials such as elastomer to PLA in a process known as rubber toughening [23,24]. Brittle PLA could be effectively toughened by blending it with a highly ductile elastomeric polymers.

Natural Rubber (NR) is an elastomeric polymer that shows many advantages including excellent mechanical properties, low cost, and ease of processing [25,26]. Most representative features of natural rubber are high elongational properties and good impact strength. Most of natural rubber sources are composed of cis-1,4-polyisoprene. Natural rubber also exhibits great elastic properties since the applied external energy is transferred to thermal energy due to the distortion of double bonds of the isoprene monomer. Some recent studies reported efficient biodegradation of NR [27]. Accordingly, NR could be used as a good toughening material for biodegradable PLA as illustrated in Figure 2.1.2. Moreover, as it comes from the rubber tree in nature, it can be used to make eco-friendly blends with biodegradable PLA.

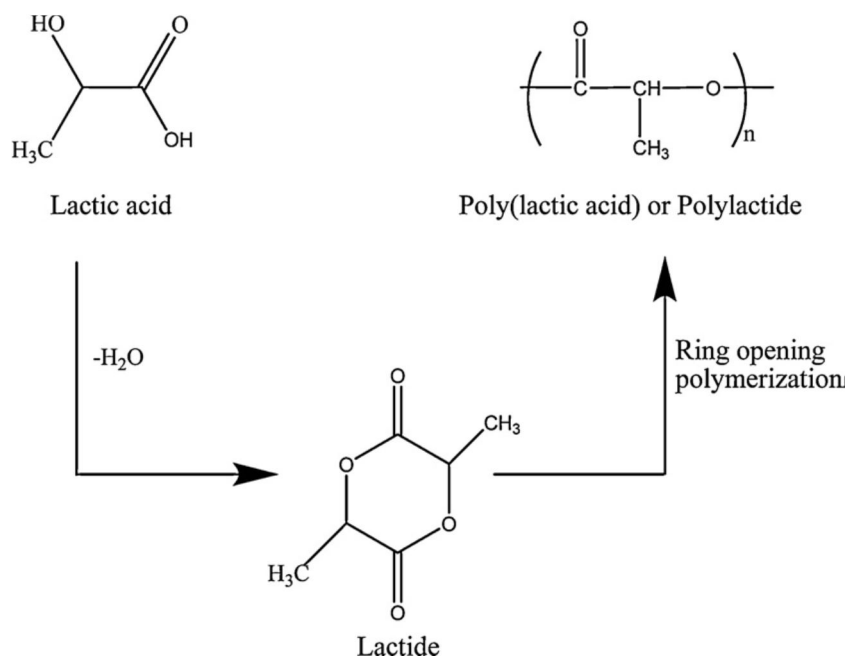


**Figure 2.1.1.** Reaction schemes to produce PLA [15,16].



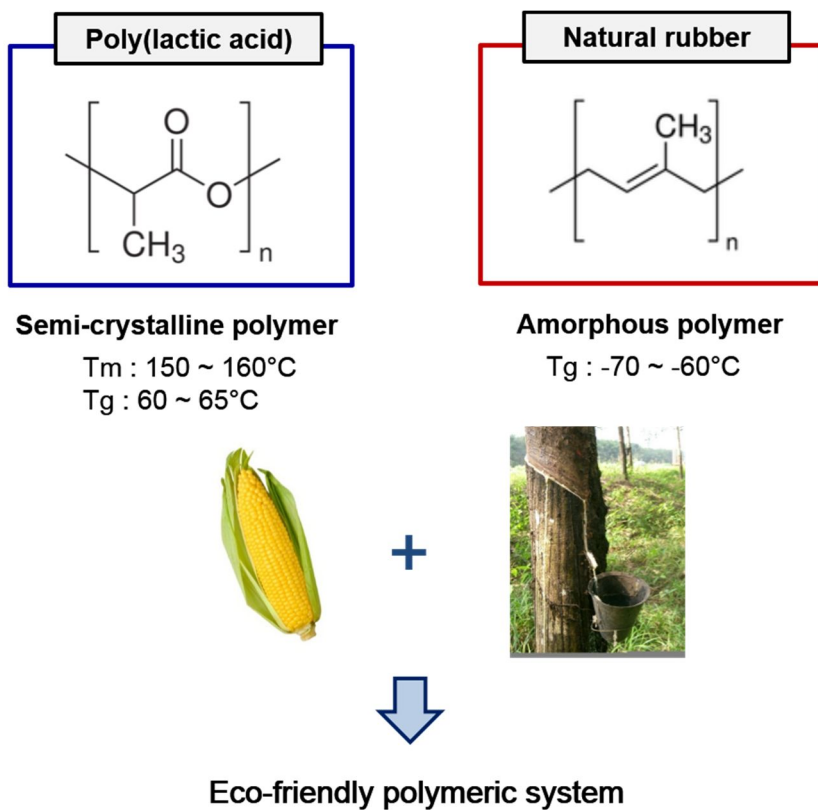


**Figure 2.1.2.** Schematic representation for structure, thermal properties, and resources of PLA and natural rubber, respectively.

## **2.2. Effect of organoclay as a compatibilizer**

However, most polymers are immiscible with others, which results in phase separation between two polymers as shown in confocal microscopy images of PLA/NR blends in Figure 2.2.1. Thus, it is essential to add a compatibilizer when two polymers are blended, copolymers being the most common ones. There have been many studies that have examined the effect of copolymers in incompatible polymer blends [28-32]. However, it is selective and sometimes expensive to find a good copolymer. Similarly, in case of PLA and natural rubber blends, maleic anhydride grafted rubber as chemical compatibilizers are usually introduced to ‘glue’ the two immiscible phases [33-35]. Such chemical compatibilizers increase manufacturing cost and introduce detrimental effects on the processability by increasing the viscosity of the blend.

Another strategy is to use inorganic solid nanoparticles as a compatibilizer. The effect of nanoparticles in polymer blends has been extensively studied. Inorganic nanoparticles could make two immiscible materials more compatible by reducing the interfacial tension of the blend [36-40]. In particular, organically modified clays (organoclays) have been actively investigated in the past few decades due to their many unique features such as large surface area and high aspect ratio [41-46]. The surface of clay can be easily modified with various functional groups with the ion exchange reaction, and one can control compatibility with many polymers. When an organoclay is added to an incompatible polymer blend, the clay particles at the interface of the two polymers reduce the drop size of the dispersed phase by lowering

the interfacial tension (Figure 2.2.2) [43,44]. As a result, the two polymers can be compatibilized. In this thesis, organically modified clays were introduced to the PLA/NR blend as compatibilizers.

The effects of organoclays on the change in various physical properties in PLA and natural rubber (NR) blends have been previously reported. Bijarimi et al. [47] reported on the crystallinity and thermal stability of the blend, and Bitinis et al. [34,35] investigated on the change in the mechanical and barrier properties according to the addition of clays in a PLA/NR blend. As shown in Figure 2.2.3, it was inferred that physical and mechanical properties of PLA/NR blends markedly improved depending on the concentration clay. However, they mainly described the change in physical properties of the blends from a macroscopic point of view, although they also investigated micromechanical deformation and reinforcement mechanisms of the PLA/NR/clay system. Also, the origin of the structural changes in the dispersed phase or of the dispersion state with different locations of organoclay has never been reported. It is important to figure out the exact mechanism for the role of organoclays as a compatibilizer in order to control the processability and to get the desirable end-use properties for industrial applications.

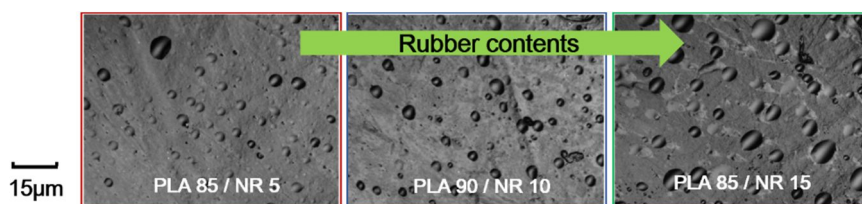


**Figure 2.2.1.** Confocal microscopy images of PLA85/NR15, PLA90/NR10, and PLA85/NR15, respectively.

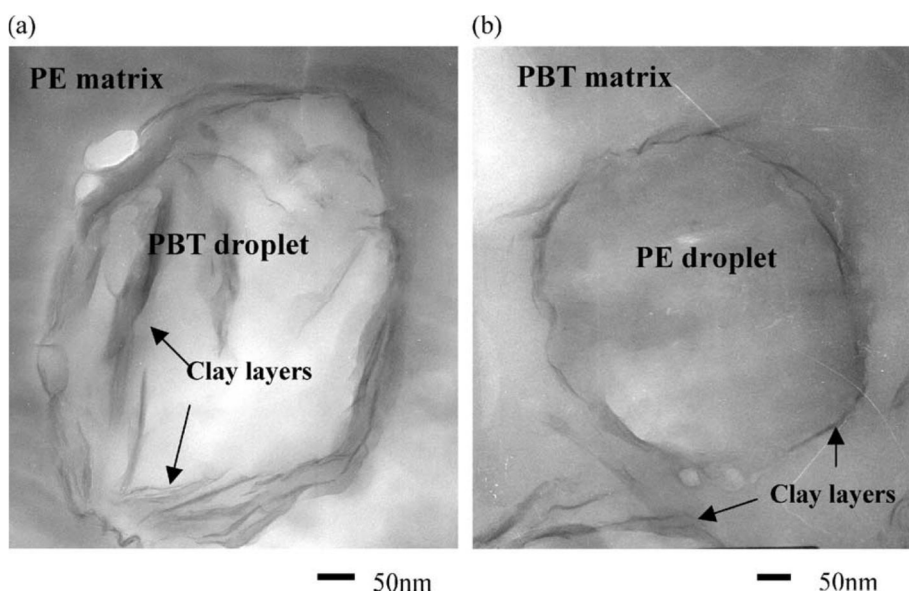


**Figure 2.2.2.** TEM pictures of 10/90 (w/w) PBT/PE (a) and 80/20 (w/w) (b) with 5 phr organoclay [43].

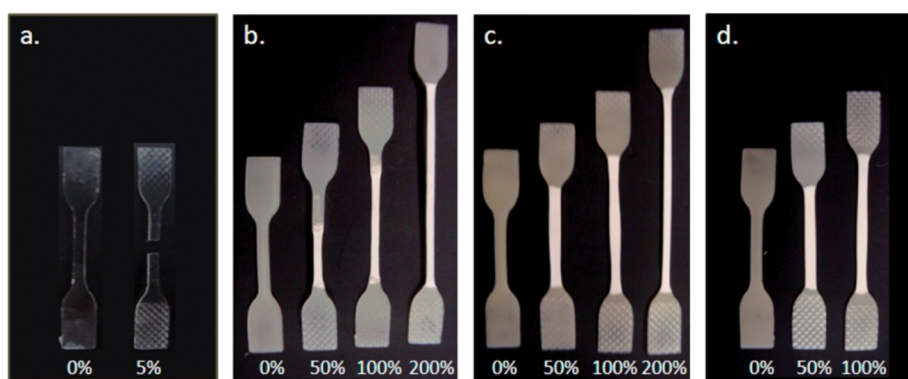


**Figure 2.2.3.** Samples stretched at different elongations (a) PLA, (b) PLA/NR, (c) PLA/NR/C15A 1wt%, (d) PLA/NR/C15A 3wt% [35].

### **2.3. Characterization of compatibilizing effect by FT-rheology**

Linear rheological material functions such as storage and loss modulus ( $G'$  and  $G''$ ) or complex viscosity ( $|\eta^*|$ ) from small amplitude oscillatory shear (SAOS) tests provide information about internal structure and properties of polymeric materials [48]. For example, the degree exfoliation of nanoclay can be determined by the increase in storage and loss modulus in polymer/clay nanocomposites [49,50]. The drop size reduction of immiscible polymer blends could also be related to the interfacial tension, which can be calculated by several mathematical models using  $G'$  and  $G''$  moduli [51]. Although many researchers have taken advantage of the linear rheological properties obtained from SAOS tests to characterize the internal structure of polymeric materials, less attention has been paid to nonlinear rheological analysis. Manufacturing process of polymers (either PLA or NR) such as injection molding, extrusion and compression molding is accompanied with very high shear or extensional flow field. In this sense, it is worth mentioning that more intensive rheological investigation should be conducted to understand the behavior PLA/NR/clay system under those types of flow field.

Among several nonlinear rheological methods, nonlinear rheological properties from large amplitude oscillatory shear (LAOS) tests have recently been of interest for characterizing complex fluids [38, 52-60]. The nonlinear shear stress response under large deformations could provide useful information regarding the topology and

morphology of polymer melt systems (i.e., polymer melts, polymer composites, and polymer blends) [57-60]. Especially, Fourier Transform rheology (FT-Rheology) has been widely used to quantify nonlinear stress responses [61-63]. As demonstrated in Figure 2.3.1, the raw stress signal as a function of time is converted to intensity as a function of frequency [64]. Among many intensities, the third relative harmonic ( $I_{3/1} \equiv I(3\omega)/I(\omega)$ , where  $\omega$  is the excitation frequency) was used as a nonlinear index. It has been reported that this index is sensitive to microstructural changes from topology to morphology of the polymer composites and blend [56].

Based on this higher sensitivity, Lim et al. proposed the Nonlinear-Linear viscoelastic Ratio ( $NLR \equiv Q_0(\phi)/Q_0(0)/|G^*(\phi)|/|G^*(0)|$ ; normalized nonlinear viscoelastic property/normalized linear viscoelastic property) as a characterization method for morphological development of various polymer nanocomposite system (Figure 2.3.2). Recently, this characterization method was utilized for detecting microstructural change of immiscible polymer blends compatibilized with organoclay. Salehiyan et al. [38,52] investigated the relationship between morphology evaluations of PP/PS blends with various compatibilizers (organoclay and silica nanoparticles) and nonlinear rheological properties from LAOS tests and found that nonlinear rheological properties were sensitive to small changes in the internal structure of polymer blends. They used NLR to quantify morphology of the PP/PS blends with various compatibilizers. As shown in Figure 2.3.3, organoclay was found to cover the PS dispersed phase at their interfaces and cause significant size reduction, which was reflected in increasing NLR values larger than 1 ( $NLR > 1$ ) [52]. They also investigated the effects of silica nanoparticles with different natures (hydrophilicity and



hydrophobicity) on PP/PS blends [38]. PP/PS blends with hydrophilic silica and no alteration of droplet size showed constant NLR values ( $\approx 1$ ) with increasing concentrations of hydrophilic silica. However, NLR values of PP/PS blends with hydrophobic silica nanoparticles were much larger than 1 ( $\text{NLR} > 1$ ), and increased with silica concentration, consistent with morphological evolution (i.e., reducing droplet size). Based on these two studies, there was an inverse correlation between NLR and droplet size.

The mechanical properties and melt strength of PLA/NR/clay were found to be increased by controlling the location of clay. When the clays were located at the interface, the drop size of natural rubber decreased greatly. It is very important to control drop size since the size of the dispersed phase plays a very important role in the final properties of the blends. In polymer blend systems, the drop size of the dispersed polymer is generally changed by the capillary number (the ratio between hydrodynamic stress and interfacial stress) and the viscosity ratio between two polymers. The droplets can be deformed and eventually broken only when the capillary number exceeds the critical capillary number [1]. In contrast, when nanoparticles are incorporated into polymer blends such as PLA/NR/clay, the morphology is not simply determined by those parameters due to the complexity in estimating hydrodynamic stress or interfacial tension.

In this respect, this thesis focused on analyzing morphological development of dispersed phase in the PLA/NR/clay system by introducing the recently proposed rheological method. In addition to the materials composition, it was investigated the

effects of mixing condition and types of clay on the morphological development and resulting properties.

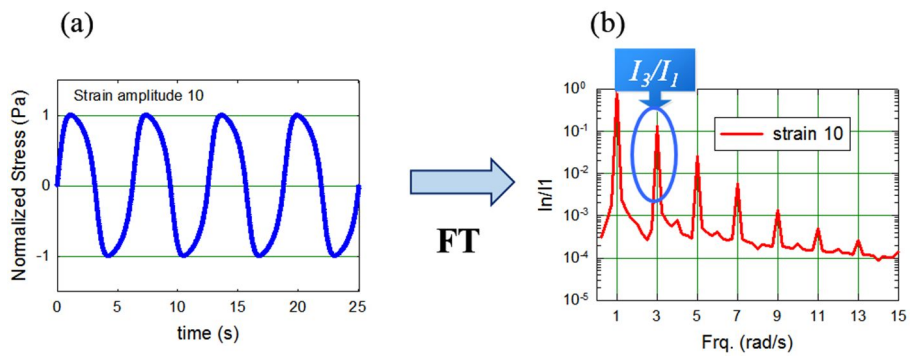


**Figure 2.3.1.** (a) Nonlinear stress curve, (b) FT-spectrum gained from FT-rheological analysis, respectively [64].

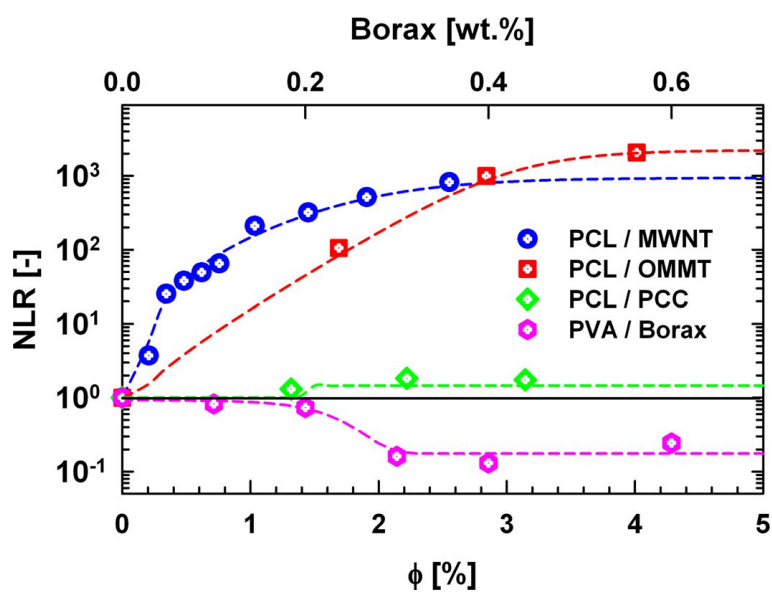


**Figure 2.3.2.** NLR of PCL/MWNT, PCL/OMMT, PCL/PCC composites, and PVA/borax solution as function of concentration. The lines are added to guide eye [59].

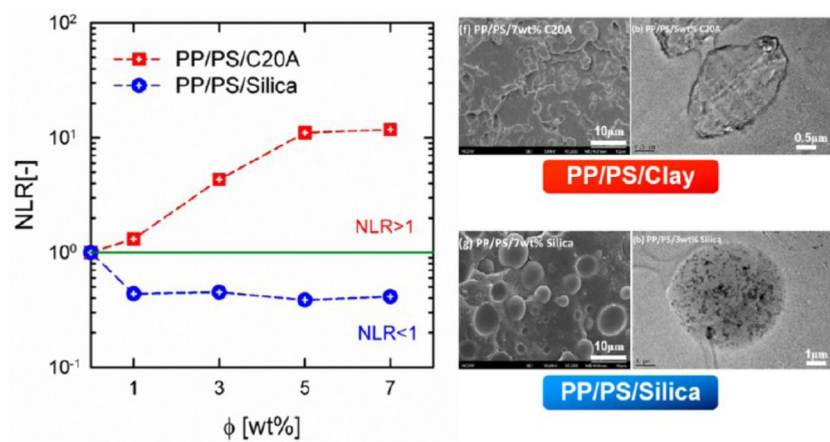


**Figure 2.3.3.** Comparison of NLR values of PP/PS/C20A and PP/PS/silica blends as a function of weight fraction of particles, and TEM images of PP/PS/ 5wt% C20A, PP/PS/ 7wt% C20A, PP/PS/ 5wt% silica, and PP/PS/ 7wt% silica, respectively [52].

## **2.4. Objectives of the thesis**

In this thesis, the mechanism of the role of organoclays as a compatibilizer in a PLA/NR blend system and the resulting microstructural development were investigated. Not only the end-use properties but also the properties of processability including the extensional viscosity were investigated to better understand the performance of the PLA/NR blend system [65]. In addition, the compatibilizing effect of organoclay in immiscible poly(lactic acid) (PLA) and natural rubber (NR) blends was characterized. The effects of clay contents, mixing conditions and types of clay on both linear viscoelastic properties from SAOS tests and nonlinear viscoelastic properties from LAOS tests were investigated. NLR was used to quantify morphological evolutions, such as the droplet size of PLA/NR blends with organoclay [66].

## **Chapter 3.**

# **Experimental methods**

### 3.1. Sample preparation

#### Raw materials

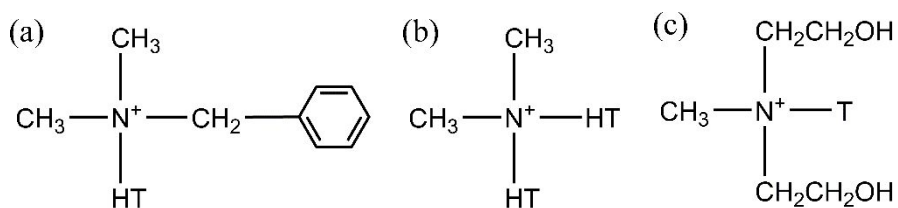
Poly(lactic acid) (PLA) used in this study is 4032D ( $\bar{M}_n = 90,000$  g/mol,  $\bar{M}_w = 181,000$  g/mol, PDI = 2.01) consisted of 98% of L-lactide and 2% of D-lactide was provided by Natureworks, USA. Natural rubber (NR), ISNR5 ( $\bar{M}_n = 260,000$  g/mol,  $\bar{M}_w = 780,000$  g/mol, PDI = 3.00, intrinsic viscosity in benzene at 30°C = 4.45 dl/g) was obtained from Rubber Board, India. The structural information about polymers used in this work is displayed in Table 3.1.1. Three different types of organoclay, Cloisite 10A (C10A), Cloisite 20A (C20A), and Cloisite 30B (C30B), were purchased from Southern Clay Products Inc., USA. The functional groups substituted on each clay surface are listed in Figure 3.1.1.

#### Blend preparation

All materials were dried in a vacuum oven at 80°C for 12 h. Blending was carried out with an intensive internal mixer (Rheocomp mixer 600, MKE, Korea) at 200°C. In order to figure out contents of organoclay on structure and properties of the PLA/NR blends for Chapter 4.1 through 4.3, Cloisite 20A (C20A) (cationic exchange capacity = 95 meq/100g clay, density = 1.77 g/cc) was chosen. The modifier of the C20A consists of two hydrogenated tallow (HT) and two methyl groups (CH<sub>3</sub>-), which shows intermediate features among three types of clays. Various concentrations of C20A particles, 0.5, 1, 2, 3, 5, and 10wt%, were added to the PLA/NR blend with a composition of 90/10 wt%. Compounding was conducted at 100 rpm in most cases,

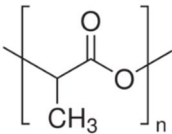
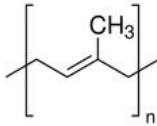
which corresponds to the shear rate  $47.1 \text{ s}^{-1}$  approximately ( $\dot{\gamma} = D\Omega/2h$ , where D is the averaged diameter of screw of the batch mixer, h is the gap between screw element and barrel,  $h=2\text{mm}$ ,  $D=36\text{mm}$  and  $\Omega$  is the rotational speed in rpm) [67,68]. The corresponding PLA/NR (9:1) blend with 3 wt% C20A was denoted PLA/NR/C20A3. For the experiments in Chapter 4.4.2, the mixing at 30, 50, and 100 rpm (corresponding to 14.1, 23.6 and  $47.1 \text{ s}^{-1}$ , respectively) was applied for PLA/NR/C20A3 to investigate the effects of mixing condition on the blends. Finally, three types of clays (C10A, C20A, and C30B) were introduced into the PLA/NR blends with a fixed concentration (3wt%) in Chapter 4.4.3. In order to avoid physical aging of PLA, rheological and mechanical properties were measured within a month after the blends were prepared.





**Figure 3.1.1.** Structures of functional groups of (a) Cloisite 10A (C10A), (b) Cloisite 20A (C20A), (c) and Cloisite 30B (C30B). T: Tallow (~65% C18; ~30% C16; ~5% C14), HT: Hydrogenated Tallow (~65% C18; ~30% C16; ~5% C14)

**Table 3.1.1.** Information of polymer used in the study.

Substance	Trademark	Structure
Poly(lactic acid) (PLA)	4032D	 $\left[ \text{CH}(\text{CH}_3)\text{COO} \right]_n$
Natural rubber (NR)	ISNR5	 $\left[ \text{CH}_2\text{C}(\text{CH}_3)=\text{CHCH}_2 \right]_n$

### **3.2. Measurement of rheological property**

A strain-controlled type rheometer, RMS 800 (Rheometrics Inc.), was used to perform rheological experiments. Linear rheological properties were obtained by frequency sweep tests within a linear viscoelastic regime. The samples were prepared using a hot press (CH4386, Carver) with a width and thickness of 25 and 1 mm, respectively. Extensional rheology measurement was done with the SER fixture on the Physica MCR 501 (Anton Paar, Austria) at 160°C and different extension rates of 0.01, 0.03, 0.07 and 0.1 s<sup>-1</sup>. Nonlinear stresses were obtained by strain sweep tests at a 1 rad/s frequency. For the raw data acquisition, a 16 bit ADC card (PCMCIA-6036E; National Instruments, Austin, USA) with a sampling rate up to 200 kHz was used. This ADC card was plugged into a laptop computer equipped with the LabView (National Instruments) software. Stress data was obtained simultaneously using an ADC card. All measurements were conducted at 190°C using a parallel plate geometry with a diameter of 25mm, similar to linear viscoelastic measurements.

### 3.3. Characterization of structure and properties of blends

#### Morphology

The morphology of pure PLA/NR blends fractured in liquid nitrogen was observed by Field Emission Scanning Electron Microscopy (FE-SEM) using a JSM 6700F at 5kV. Transmission Electron Microscopy images were taken using a JEM 2100F at an accelerating voltage of 200 kV for PLA/NR/clay. Samples were prepared by cryotomy after being molded in epoxy resin. The number averaged diameter ( $D_n = \frac{\sum n_i D_i}{\sum n_i}$ ), volume-to-surface averaged diameter ( $D_{vs} = \frac{\sum n_i D_i^3}{\sum n_i D_i^2}$ ), the weight averaged drop diameter ( $D_w = \frac{\sum n_i D_i^2}{\sum n_i D_i}$ ), the volume averaged diameter ( $D_v = \frac{\sum n_i D_i^4}{\sum n_i D_i^3}$ ), interparticle distance ( $ID = d_w \left[ \left( \frac{\pi}{6\phi} \right)^{1/3} - 1 \right]$ ) and polydispersity index ( $PI = D_{vs}/D_n$ ) were estimated measuring at least 100 droplets using the Image J software.

#### Tensile test

The tensile test was conducted following the ASTM D638 type V with UTM (LF plus, Lloyd instruments Ltd). The experiments were repeated 10 times, and the data were averaged.

#### X-ray diffraction

X-ray diffraction analysis was done with the D / MAX-2500 (RIGAKU, Cu-K $\alpha$  radiation,  $\lambda = 1.5418$  with an acceleration voltage of 40 kV). The diffraction spectrum within  $2\theta$  range between  $1.2^\circ$  and  $10^\circ$  was analyzed.

## **Chapter 4.**

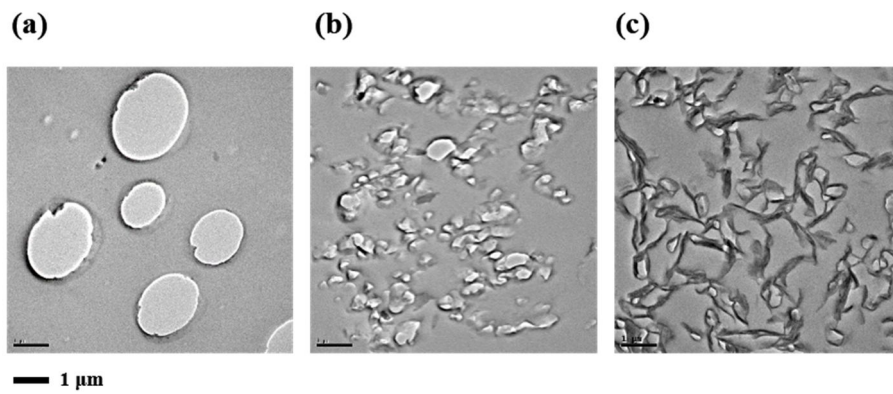
### **Results and discussion**

## 4.1. Microstructure of PLA/NR/clay

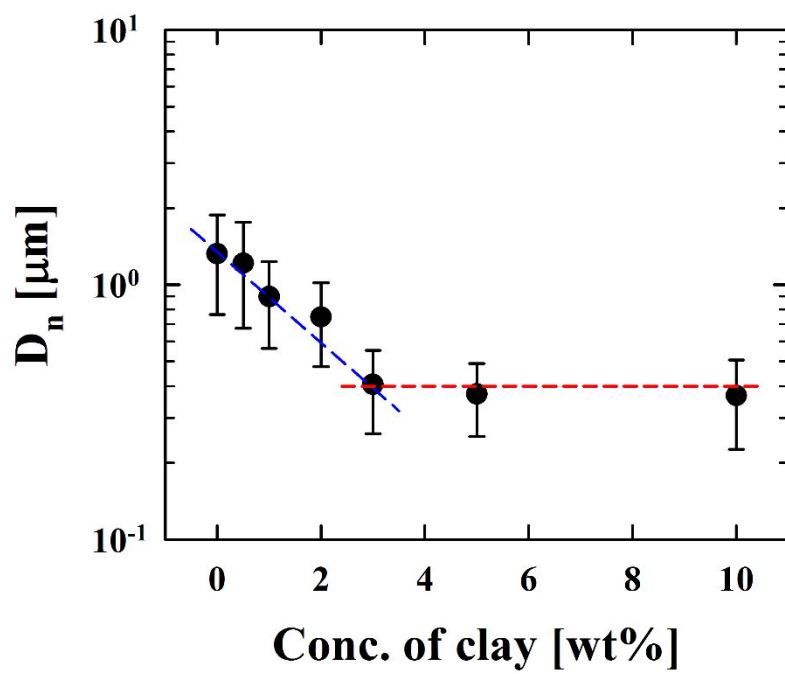
### 4.1.1. Morphological development

Figure 4.1.1 shows the TEM images of three representative blends (PLA/NR, PLA/NR/C20A3 and PLA/NR/C20A10). The images clearly show that the NR droplets are uniformly distributed and stabilized inside the PLA matrix. The size of the dispersed NR phase dramatically decreases with the increase in clay concentration. Quantitative analysis of the TEM images are presented in Figure 4.1.2. The number averaged diameter ( $D_n$ ) is plotted as a function of clay content. The drop size shows a clear concentration dependence. As the clay content increases, the  $D_n$  decreases and levels off to a constant after 3wt%. The weight averaged diameter ( $D_w$ ) shows a similar trend. At clay concentrations lower than 3wt%, the clay particles are rarely observed; however, they are clearly observed in the PLA domain for a clay content of 10wt%.

The location of the clay changes depending not only on the affinity between the polymer and clay but also on the clay content in the immiscible polymer blend system, resulting in different physical properties and structures of the blend [43]. Thus, the selective position of the clays in addition to the size of the dispersed phase was observed using high-magnification TEM images.



**Figure. 4.1.1.** Transmission Electron Microscopy (TEM) images of (a) PLA/NR, (b) PLA/NR/C20A3, and (c) PLA/NR/C20A10.



**Figure 4.1.2.** Number-averaged diameter ( $D_n$ ) of the PLA/NR blends as a function of clay content.



### 4.1.2. Selective localization and dispersion quality of clay

As shown in Figure 4.1.3, the clay particles exist mostly at the interface of the two polymers for a clay content of 0.5~3wt%. At concentrations higher than 5wt%, the organoclays exist even in the PLA phase. In the case of PLA/NR/C20A5, the clay forms a core-shell like structure surrounding the interface. When the clay content reaches 10wt%, a significant amount of clay particles exit in the PLA domain forming a branched structure. To estimate the selective location of organoclays in PLA/NR blends, wetting coefficient was calculated.

$$\omega_a = \frac{\gamma_{\text{Clay-PLA}} - \gamma_{\text{Clay-NR}}}{\gamma_{\text{PLA-NR}}} \quad (4.1.1)$$

where  $\gamma_{\alpha-\beta}$  is the interfacial tension between the material  $\alpha$  and  $\beta$ .

The clay would be localized at the interface if  $|\omega_a| < 1$ . The surface tension is 30.81 mN/m for PLA, 16.75 mN/m for NR and 25.44 for C20A [34, 69-71], from which the interfacial tension was evaluated. According to the calculation, the wetting coefficient ( $|\omega_a|$ ) was 0.3047. This result implies that the clays are preferentially localized at the interface, which results in the reduction of the interfacial tension and prevents coalescence, so that the size of the droplet does not increase any more.

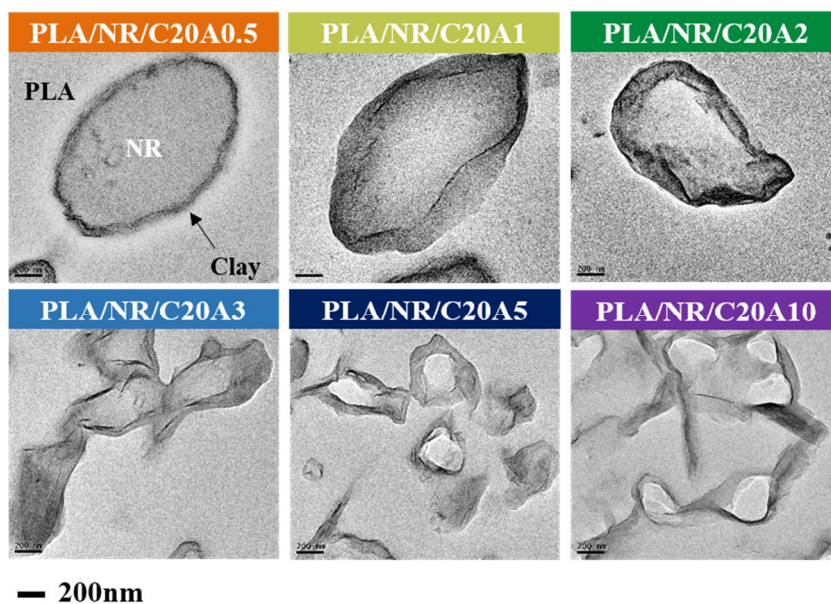


**Figure 4.1.3.** TEM images of the PLA/NR blends with different clay concentrations (0.5~10wt%).

In Figure 4.1.4, the PLA/NR/C20A0.5 and PLA/NR/C20A1 do not show any distinct  $2\theta$  peak of pristine C20A ( $3.23^\circ$ ). The disappearance of distinct peak of the pristine clay in XRD pattern originates from the change in structural regularity of silicate layers, which implies that the distance between silicate layers in the PLA/NR blend becomes larger than that of the pristine clay, indicating highly disordered structure. Therefore, the disappearance of the clay peak in XRD can be related to the exfoliation of clays at the interface between the two polymers. This result is in a good agreement with the TEM morphology. The  $2\theta$  peak begins to appear when the clay content is about 3wt%, and it is clearly observed above a clay concentration of 5wt% for which the d-spacing changes from 1.8 nm to 1.37 nm. The decrease of the  $2\theta$  angle suggests that the distance between the clay layers increases because the polymer chains intercalate into the clay galleries.

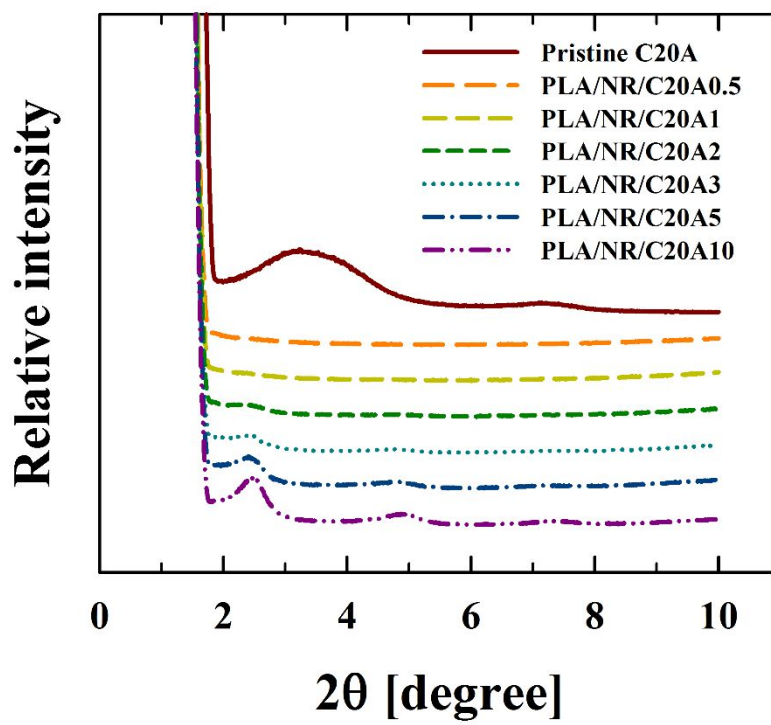


**Figure 4.1.4.** XRD patterns of pristine C20A, PLA/NR and PLA/NR/C20A with different clay contents (0.5~10 wt%).

## 4.2. Linear rheological analysis

### 4.2.1. Dynamic properties

Storage and loss moduli of the PLA/NR blends with varying clay content are shown in Figure 4.2.1(a) and (b). Those of PLA/NR show a strong frequency dependence with a typical terminal behavior at low frequencies. In contrast,  $G'$  and  $G''$  of PLA/NR/C20A show a weak frequency dependence and increase with the clay content. As demonstrated in Figure 4.2.1(c), the complex viscosity of PLA/NR blends increases with clay content while the frequency dependence is more pronounced with the added clays. For example, the  $\eta^*$  at 0.1 rad/s of PLA/NR/C20A10 ( $154 \times 10^3$  Pa-s) is enhanced approximately 216 times higher than that of PLA/NR (713 Pa-s) as listed in Table 4.2.1.

One of the reasons for this change is the increase of the surface area due to the reduction in drop size in the dispersed phase [44]. The moduli of the blends also increase even with a clay content larger than 3wt%, at which the drop size of NR becomes saturated. In addition, all the blends except for PLA/NR/C20A0.5 show the crossover point ( $G'=G''$ ). These results indicate that the increase in moduli as well as complex viscosity of PLA/NR/C20A is caused by the formation of network structures.

For the blends containing 0.5~3wt% of clay, the moduli at the low frequency region increase rapidly, and the terminal slope levels off gradually with the clay content as well, which is caused by the formation of a 3-D percolation structure [72]. This non-terminal behavior at the low clay content indicates that the percolation

network is formed due to the clays at the interface. On the other hand, the moduli of PLA/NR/C20A5 and PLA/NR/C20A10 increase even at high frequencies, which is caused by the filler effect of the excess clays in the matrix phase. All the clays are located at the interface or inside NR phase as evidenced by the TEM morphology. The dispersion state of the clay is either exfoliated or intercalated according to the XRD analysis. In addition,  $\tan \delta$  ( $G''/G'$ ) at 0.1rad/s decreases with the clay content, reaching a plateau after 3wt% (Figure. 4.2.2). The blend is liquid-like at a low clay content, but it becomes solid-like at a clay content of 2~3wt%.

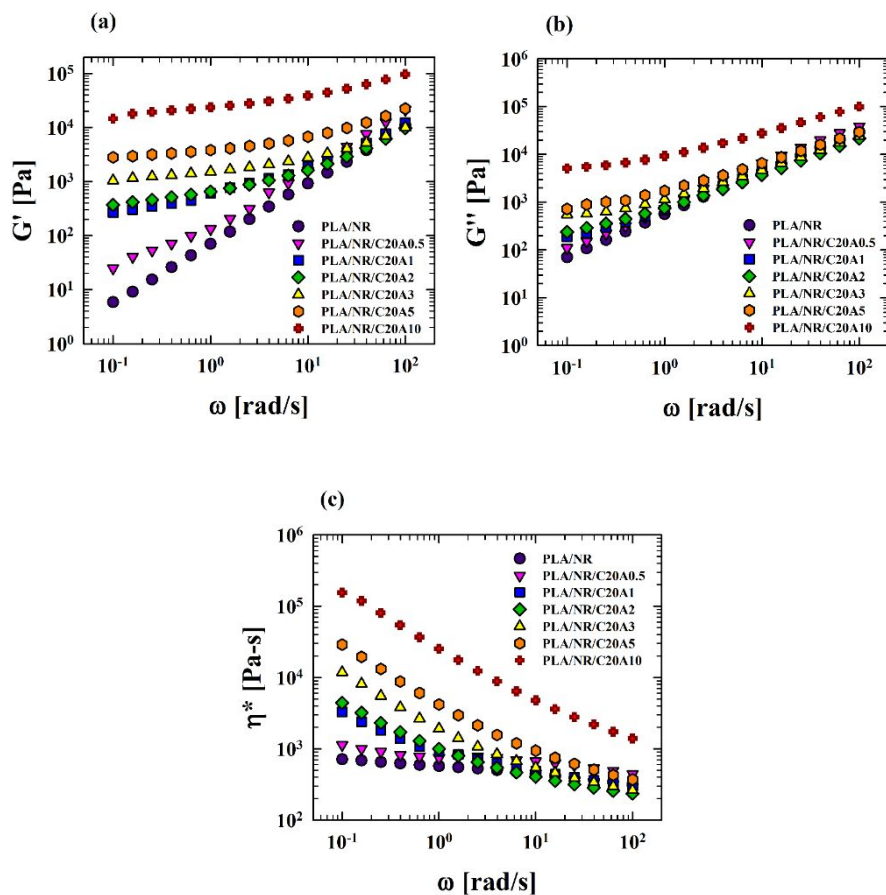


**Figure 4.2.1.** (a) Storage modulus ( $G'$ ), (b) loss modulus ( $G''$ ) and (c) complex viscosity ( $\eta^*$ ) of PLA/NR and PLA/NR/C20A as a function of angular frequency measured at 190°C.

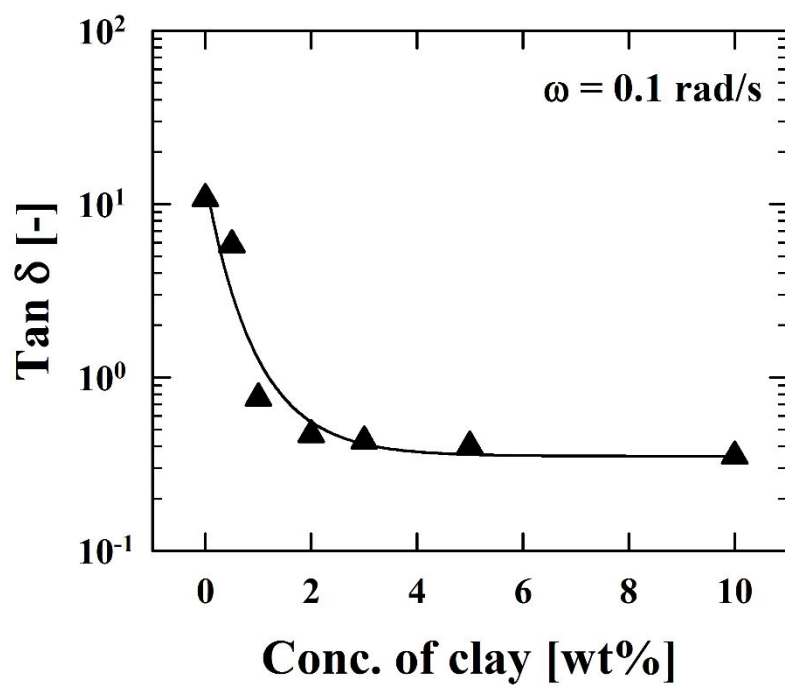


**Figure 4.2.2.**  $\tan \delta$  of the PLA/NR/clay at 0.1 rad/s depending on the concentration of the clay (0~10 wt%).



**Table 4.2.1.** Complex viscosity at 0.1 rad/s and terminal slope of the PLA/NR blends with different contents of organoclay.

Organoclay [wt%]	$\eta^*$ at 0.1rad/s [Pa-s]	Slope [-]
0	713	-0.09
0.5	1,131	-0.10
1	3,278	-0.45
2	4,400	-0.57
3	11,816	-0.73
5	28,983	-0.80
10	154,262	-0.80

#### 4.2.1.1. Interfacial tension

The Palierne model (Eq. 4.2.1) is introduced to calculate the interfacial tension between the matrix phase and the dispersed phase [51].

$$\tau_1 = \frac{D_v \eta_m}{4\alpha} \frac{(19K+16)(2K+3-2\phi(K-1))}{10(K+1)-\phi(5K+2)} \quad (4.2.1)$$

Here,  $\tau_1$  is the interfacial relaxation time,  $K$  is the ratio of the viscosity of the dispersed phase ( $\eta_d$ ) and that of the matrix ( $\eta_m$ ),  $\alpha$  is the interfacial tension, and  $\phi$  is the volume fraction of the dispersed phase. The interfacial relaxation time is determined by the weighted relaxation spectrum, which is obtained from the linear viscoelastic properties using the fixed-point iteration method proposed by Cho and Park [73,74]. As shown in Figure 4.2.3(a), the relaxation times of neat PLA and NR are about 0.01s and 0.67s, respectively. For PLA/NR, the first peak appears at 0.2s and the second peak at 2.7s. In general, the longest relaxation time, except for the peaks corresponding to the relaxation time of either the matrix phase or the dispersed phase, is known as a characteristic time for the interfacial relaxation [75,76]. The relaxation spectra of PLA/NR (Figure 4.2.3(a)) show two peaks. The spectra of PLA/NR/20AC (i.e., PLA/NR/C20A2 in Figure 4.2.3(b)) also have two peaks, with a more intense second peak.

When the clay content increases, the time at which the second peak appears also increases (Table 4.2.2). The intensity becomes stronger with the increase in clay content as well (Fig. 4.2.3(b) inset). These results demonstrate that the second peak of

the spectra corresponds to the longest relaxation time reflecting the characteristics of the relaxation behavior of the interface. Then, it can be concluded that the first peak corresponds to the neat NR, while the relaxation time of PLA is shifted to a lower time, not shown in this spectra. The shift of the relaxation time might be caused by the complex internal structure of the incompatible PLA/NR blends.

For the blends with a clay content between 1 and 3 wt%, which exhibit a clear weighted relaxation spectrum, the interfacial tension can be calculated. The longest relaxation time ( $\tau_1$ ) and the volume averaged drop size ( $D_v$ ) as well as the calculated interfacial tension ( $\sigma$ ) from Eq. 4.2.1 are shown in Table 4.2.2. The interfacial tension of the PLA/NR is about 1.50 mN/m, gradually reducing to 0.86 mN/m for PLA/NR/C20A1 and 0.26 mN/m for PLA/NR/C20A3. When the clay is added to the immiscible polymer blends, two polymers are adsorbed on the clay surface. This results in a gain in the stabilization energy, which leads to a decrease of the drop size as well as the interfacial tension [43]. The interfacial tension in this case is reduced due to the role of the clay as a compatibilizer. Therefore, it is expected that the excess amount of clay which is located in the matrix phase does not affect the formation of the interface. In other words, the extra addition of the clay does not affect the interfacial tension of the blends. Therefore, it is reasonable to assume that the interfacial tension of PLA/NR/C20A5 and PLA/NR/C20A10 is identical to that of PLA/NR/C20A3.

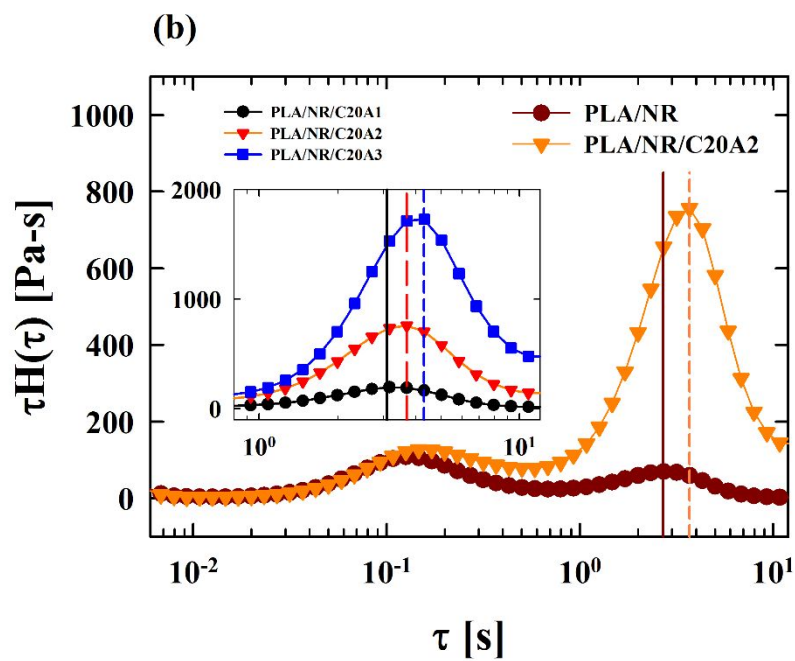
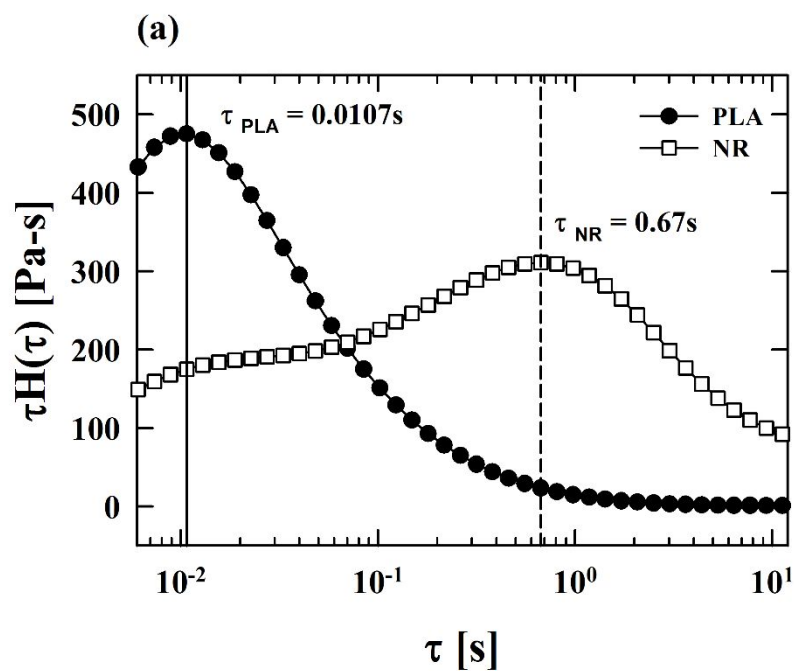


**Figure 4.2.3.** Weighted relaxation spectrum of (a) neat PLA and NR, and (b) PLA/NR and PLA/NR/C20A2. Inset: the spectrum of PLA/NR/C20A1, PLA/NR/C20A2 and PLA/NR/C20A3 in the high relaxation time regime.

**Table 4.2.2.** Interfacial tension between PLA and NR and the parameters used to calculate it.

Organoclay [wt%]	$R_v$ [ $\mu\text{m}$ ]	$\tau_1$ [s]	$\alpha$ [mN/m]
0	1.96	2.70	1.50
1	1.31	3.17	0.86
2	1.03	3.69	0.58
3	0.53	4.30	0.26
5	0.48	-	0.26
10	0.51	-	0.26

#### 4.2.1.2. Capillary number estimation

The size of the dispersed phase is determined by two dimensionless numbers, the viscosity ratio between the dispersed phase and the matrix phase and the capillary number (Eq. 4.2.2) in incompatible polymer blends [1].

$$Ca = \frac{\text{hydrodynamic stress}}{\text{interfacial stress}} = \frac{\eta_m \dot{\gamma} R}{\alpha} \quad (4.2.2)$$

where  $Ca$  is the capillary number,  $\eta_m$  is the viscosity of the matrix,  $\dot{\gamma}$  is the shear rate,  $R$  is the drop size of the dispersed phase,  $\alpha$  is the interfacial tension.

Drop deforms only when the capillary number ( $Ca$ ) is larger than the critical capillary number ( $Ca_{crit}$ ) at a specific viscosity ratio. When  $Ca$  is larger than  $Ca_{crit}$ , the droplet breaks up. At high shear stress, the capillary number increases and accelerates the breakup process of the dispersed phase. The finely broken droplets cause a high surface energy, resulting in a thermodynamically unstable state. Therefore, the droplets combine with each other in order to lower the surface energy of the system [77]. Once the interfacial tension (Table 4.2.2) and the other parameters (Table 4.2.3) were calculated, capillary number was estimated. It may be named as a nominal capillary number ( $Ca_n$ ) due to several assumptions as following (Table 4.2.4).

The  $Ca_n$  of the PLA/NR/clay is plotted with the viscosity ratio in Figure 4.2.4. Below the critical clay contents, the capillary number increases due to the decrease in interfacial tension. As a result, the droplet breakup is more accelerated. The clay is

found to be selectively localized at the interface below 3wt%, as illustrated in Figure 4.1.3. On the other hand, as the clay content increases further (PLA/NR/C20A5 and PLA/NR/C20A10), the clay exists in the PLA phase too. This is in good agreement with previous reports by Hong et al. [43,44]. In this case, the capillary number also increases as the clay concentration increases. However, the viscosity ratio between the dispersed phase and the matrix phase decreases due to the excess amount of clay in the matrix phase, resulting in higher  $Ca_{crit}$  for the breakup of drops.

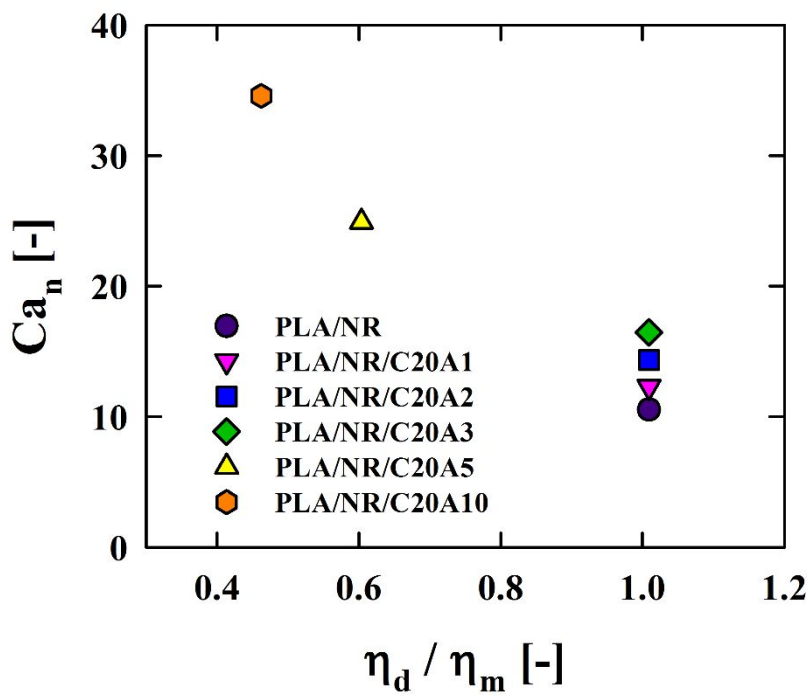


**Figure 4.2.4.** Estimated nominal capillary number ( $Ca_n$ ).



**Table 4.2.3.** Viscosity of the dispersed phase and the matrix phase and their ratio at a given shear rate ( $47.1 \text{ s}^{-1}$ ) depending on the clay content in the PLA / NR blends.

Clay contents [wt%]	$\eta_d$ [Pa-s]	$\eta_m$ [Pa-s]	$\eta_d/\eta_m$ [-]
0	415	343	1.01
1	377	343	1.01
2	346	343	1.01
3	313	343	1.01
5	313	573	0.60
10	313	748	0.46

**Table 4.2.4.** Assumptions made to calculate nominal capillary number

Assumptions
<ul style="list-style-type: none"><li>• Shear viscosity can be replaced by complex viscosity according to Cox-Merz rule [78].</li></ul> $\eta(\dot{\gamma}) =  \eta^*(\omega) _{\dot{\gamma}=\omega}$ <ul style="list-style-type: none"><li>• Shear rate is defined by <math>\dot{\gamma} = D\Omega/2h</math>, where D is the diameter of a blade, h is the gap between blade and wall, and <math>\Omega</math> is the rotation speed in rpm. As h=2mm, D=36mm in this case, 100 rpm corresponds to shear rate <math>47.1 \text{ s}^{-1}</math> [67,68].</li><li>• The maximum loading of the clay at the interface is 3wt%, above which extra clay locates only in the matrix phase (PLA).</li><li>• When the clay locates at the interface, it does not affect the viscosity ratio between PLA and natural rubber.</li></ul>

### 4.2.1.3. Effect of clay exfoliation

The drop size of the dispersed phase and resulting rheological properties of PLA/NR/clay blend are closely related to clay exfoliation. The rheological evidences such as strong shear thinning in complex viscosity and decrease in terminal slope of storage and loss moduli shown in Figure 4.2.1 imply the enhanced degree of exfoliation [79,80]. The storage modulus of PLA/NR without clay is almost same with that of neat PLA, but their change to the addition of clay is dramatically different, which is also evidenced by the different size of clay tactoids. TEM images demonstrate that the thickness of clay tactoid is about  $\sim 0.7 \mu\text{m}$  for PLA/clay (Figure 4.2.5(a)), whereas it decreases down to  $\sim 10 \text{ nm}$  for PLA/NR/clay (Figure 4.2.5(b)).

To separate the effect of clay exfoliation, the ratio between the normalized modulus of PLA/NR/clay and that of PLA/clay is introduced.

$$\Psi = \frac{[G'_0(\phi)/G'_0(0)]_{\text{PLA/NR/clay}}}{[G'_0(\phi)/G'_0(0)]_{\text{PLA/clay}}} \quad (4.2.3)$$

where  $G'_0$  is  $G'$  at  $0.1 \text{ rad/s}$  and  $\phi$  is the clay concentration.

The  $\Psi$  value increases dramatically between 0.5 and 1wt%, and then decreases asymptotically to a constant value after 3wt% as shown in Figure 4.2.6. The sudden increase in  $\Psi$  is related to the increase in the degree of exfoliation. Below 1 wt%, the clay shows fully exfoliated structure at the interface between PLA and NR, whereas

the blend contains both exfoliated and intercalated structures at the interface for PLA/NR/C20A2 and PLA/NR/C20A3, as evidenced in Figures 4.1.3 (TEM) and 4.1.4 (XRD). Over 5 wt%, the extra clays in the matrix would form tactoids or intercalated structures, which leads to small  $\Psi$ .

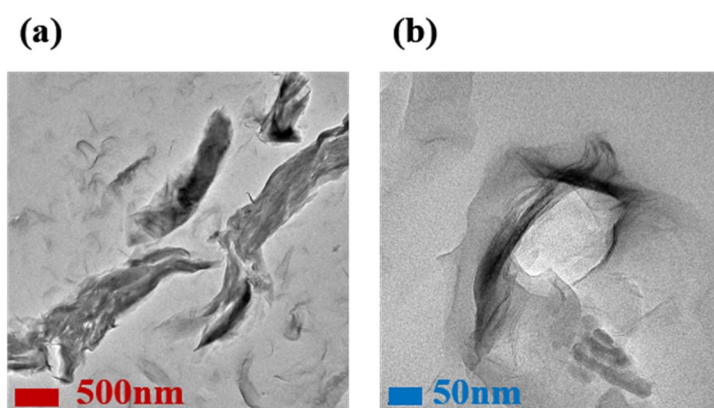


**Figure 4.2.5.** TEM images for (a) PLA/C20A3 and (b) PLA/NR/C20A3. Scale bar is 500nm for (a) and 50nm for (b).

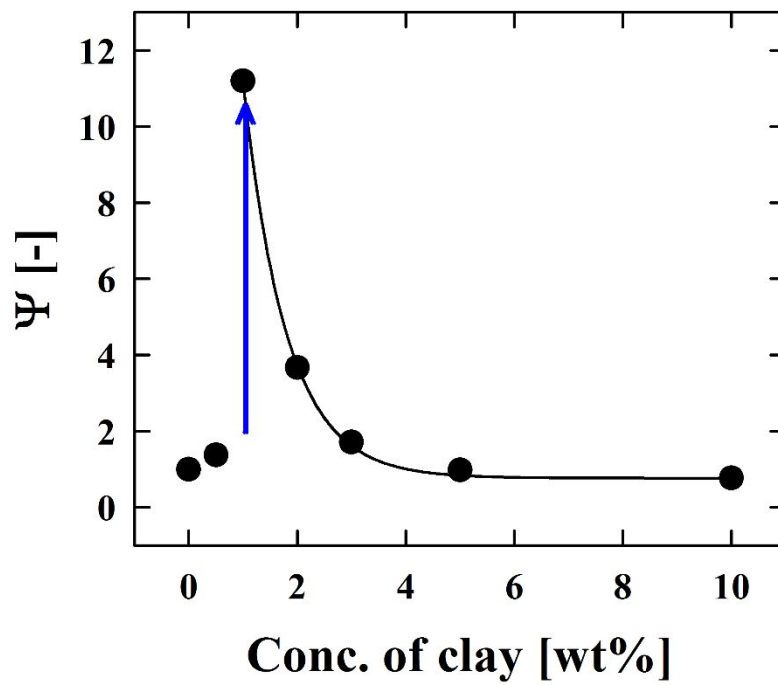


**Figure 4.2.6.**  $\Psi$  as a function of clay content.

## 4.3. Elongational rheology

### 4.3.1. Extensional viscosity

The transient extensional viscosities of the pure PLA and PLRC under various extension rates (0.01, 0.03, 0.07 and 0.1 s<sup>-1</sup>) are shown in Figure 4.3.1. The extensional viscosity of the neat PLA increases with time, following the  $3\eta_0$  curve (Eq. 4.3.1), solid line in Figure 4.3.1), as expected.

$$\eta_E(\dot{\epsilon})\dot{\epsilon} = 3\eta(\dot{\gamma})\dot{\gamma}|_{\dot{\epsilon}, \dot{\gamma} \rightarrow 0} \quad (4.3.1)$$

where  $\eta_E$  is the extensional viscosity,  $\eta$  is the shear viscosity,  $\dot{\epsilon}$  is extensional rate, and  $\dot{\gamma}$  is the shear rate.

Additionally, the time at which the strand ruptures decreases as the extension rate increases. The strain at the rupture is approximately constant irrespective of the extension rates. Strain-hardening is observed in PLA/NR/C20A0.5 and PLA/NR/C20A1, but it is most remarkable at clay concentrations of 2~3wt%. The strain for the breakup of the specimen is larger than that of neat PLA. However, the strain-hardening behavior disappears in the blends with a clay content larger than 5wt%. The Trouton ratio (Tr: the ratio of the extensional viscosity to shear viscosity) for each blend is given in Figure 4.3.2, showing the trend for the extensional behavior of the blends according to the clay content. When the clay content is less than 3wt%,

strain-hardening is caused by the exfoliated clays at the interface. In contrast, the hardening behavior becomes weak and eventually disappears due to the excess amount of clays in the matrix phase acting as a stress point.



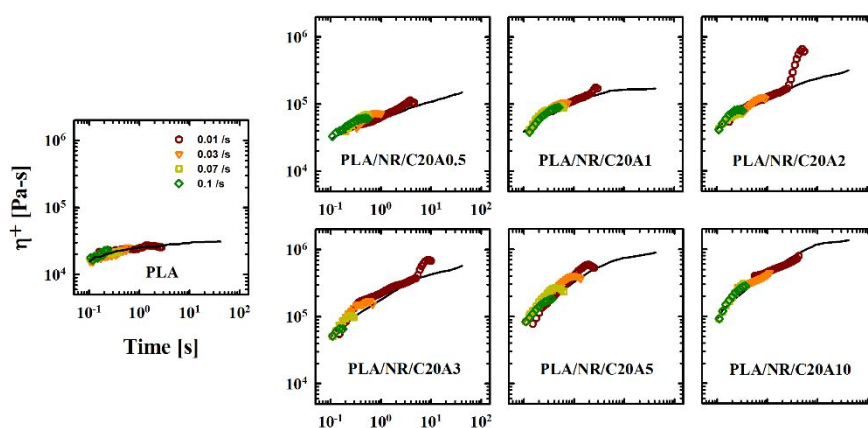


**Figure 4.3.1.** Transient extensional viscosity as a function of time for the neat PLA and PLA/NR/C20A measured at 160°C.

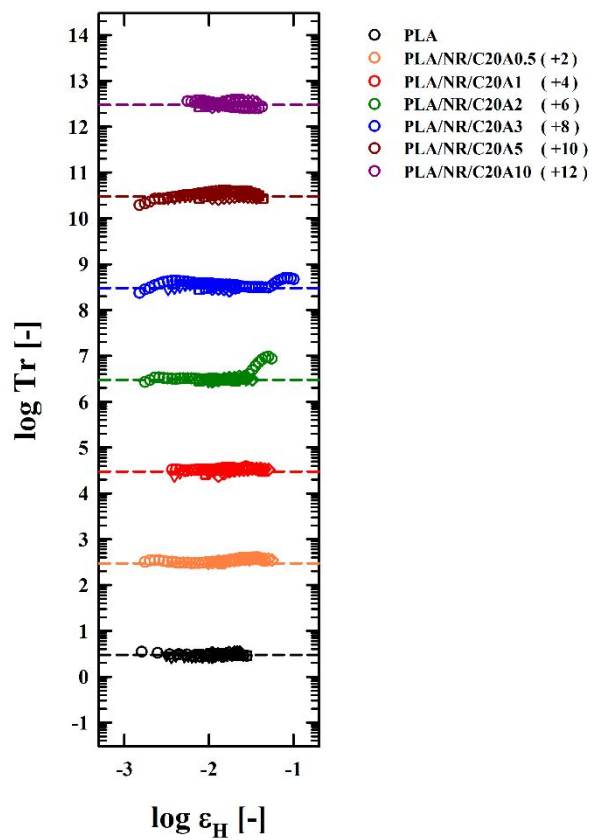


**Figure 4.3.2.** Trouton ratio of the neat PLA and PLA/NR/C20A with different clay content (0.5~10 wt%).

### 4.3.2. Mechanical properties

The mechanical properties of the blends are shown in Figure 4.3.3. The elongation at break of the blends with a clay content of 0.5~3wt% is much larger than that of PLA/NR. However, when the content is higher than 5wt%, the strain is reduced. This transition of the tensile strain with respect to the clay content can be attributed to the different role of the clay on the mechanical properties according to its selective localization. Meanwhile, the tensile strength of the blend decreases significantly with the addition of clay up to 1wt%, and changed little with further clay content. Wu et al. explained the mechanism of rubber toughening in a polymer blend system [81,82]. When rubber is introduced as a toughening material in a matrix polymer, the interparticle distance decreases and the van der Waals attraction between the particles increases, which results in the increase in yielding behavior. The interparticle distance (ID) between the dispersed droplets is first reduced and then reaches to a constant value (about 0.2  $\mu\text{m}$ ) for a clay content near 3wt% (Figure 4.3.4). Below the critical concentration (3wt%), the elongational strain increases following the rubber-toughening mechanism. After the threshold amount of clay, despite the minimum ID value, the properties of the blends become more brittle again because the clays in a matrix phase act as the stress point under the flow field. Thus, it is suggested that the final properties of the immiscible polymer blend system can be designed by controlling the localization of the clays in the blend system and their different roles depending on the clay content.

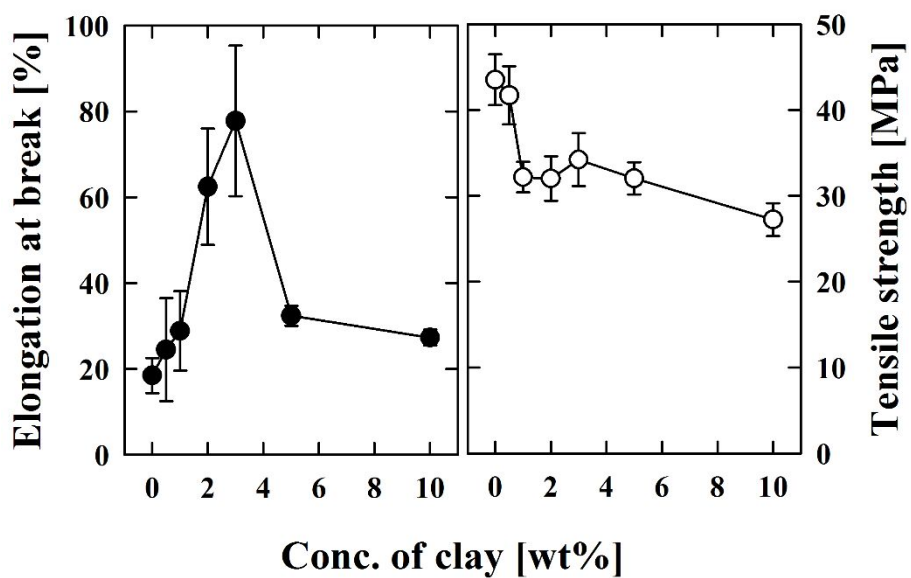


**Figure 4.3.3.** Elongation at break and tensile strength of the PLA/NR blend and PLA/NR/C20A measured at room temperature.

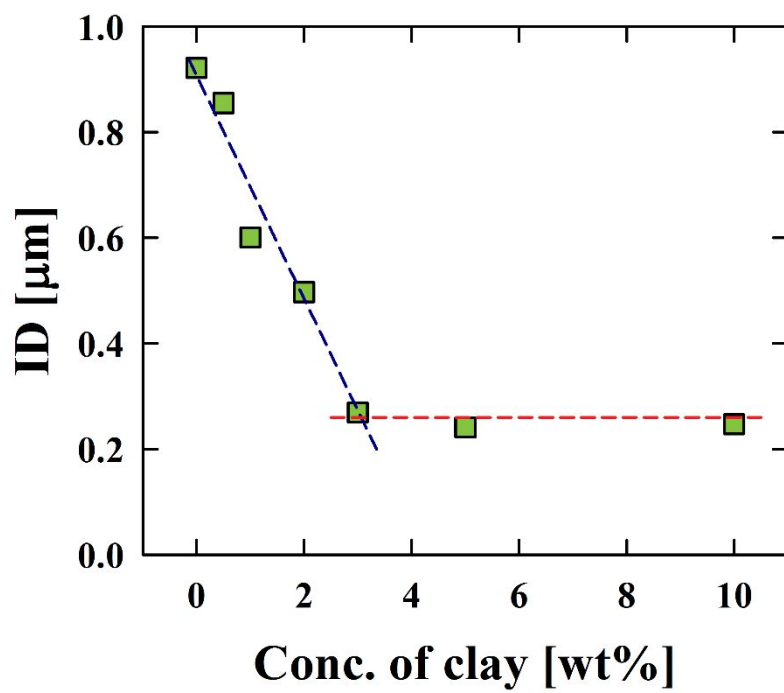


**Figure 4.3.4.** Interparticle distance of the PLA/NR/C20A as a function of clay concentration.

## 4.4. Nonlinear rheological characterization

### 4.4.1. Concentration of clay

In Figure 4.4.1, the linear rheological properties of PLA90/NR10 blends with different C20A contents measured from small amplitude oscillatory shear (SAOS) tests are plotted. Figure 4.4.1(a) shows the complex moduli ( $|G^*|$ ) of the PLA/NR/C20A blends. The complex modulus of the blend gradually increased as the clay content increased. Especially, the  $\log |G^*|$  at 0.1 rad/s highly increased as the clay contents increased (Figure 4.4.1(b)). The terminal complex modulus at 0.1 rad/s was proportional to the power of clay contents ( $\log |G^*| \sim c^n$ ). At clay contents lower than 3wt% (Regime I in Figure 4.4.1(b)),  $|G^*|$  increased with increasing clay levels ( $n=0.37$ ). However, the modulus increased with a slope of 0.16 at above 3wt% of clay (Regime II in Figure 4.4.1(b)). The terminal slope for complex moduli rapidly decreased with the clay content and became almost constant above 3wt%, displaying a certain transitional behavior of the PLA/NR blends depending on the clay content. As depicted in Figure 4.4.1(c) and (d), storage ( $G'$ ) and loss ( $G''$ ) moduli of the blends at various frequencies (0.1, 1, 10, and 100 rad/s) also vary at around the clay contents of 3wt%, similar to the tendency of the complex moduli. The different trends of linear viscoelastic properties according to the clay concentration suggest that the structure of the blends varies with clay contents.

In general, increases in the moduli of the complex system (i.e., polymer nanocomposites, polymer blends, particulate suspension, etc.) in the terminal region

strongly reflect formation of networking between components. In case of polymer nanocomposite system, interaction between nanoparticles as well as their dispersion quality strongly affect this nonterminal behavior, whereas it is highly affected by increased interfacial area for compatibilized polymer blends [45, 83]. The material system in this study is called polymer blend nanocomposite which contains two polymers and one particle together. It is difficult to explain effects of each component separately on structural change only with linear rheological material functions in SAOS test such as  $G'$ ,  $G''$  and  $G^*$  due to the complexity of the PLA/NR/clay. For a clear understanding of structural development of the blends, an advanced rheological analysis beyond dynamic modulus analysis is essential.

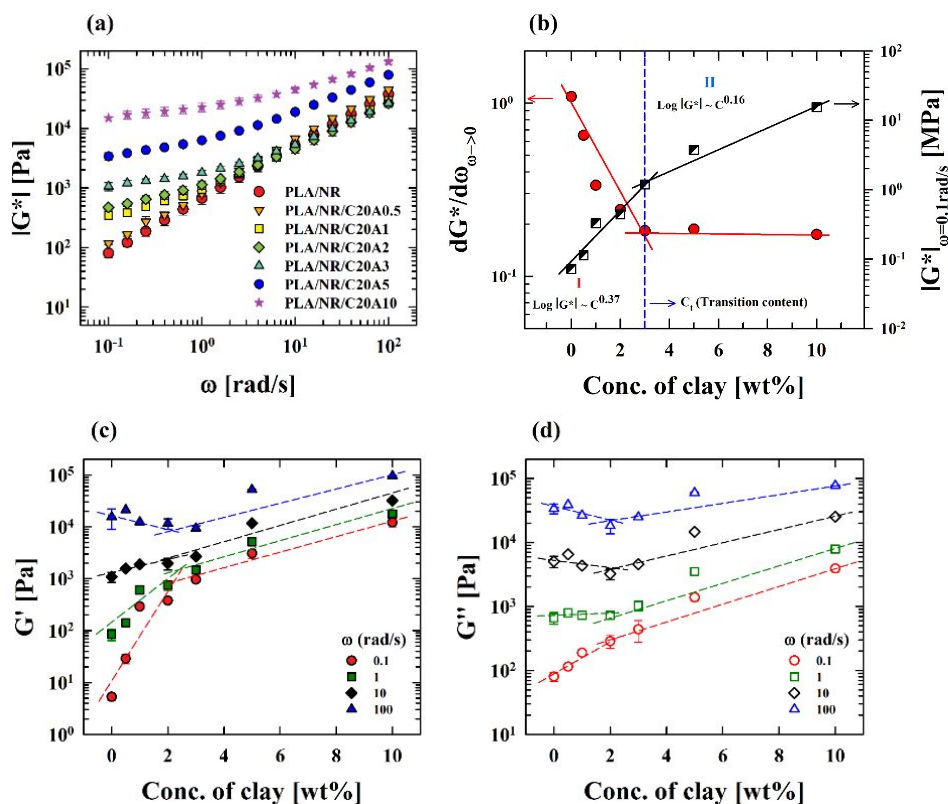


**Figure 4.4.1.** Linear rheological properties of PLA/NR blends filled with various concentrations of C20A particles, 0, 0.5, 1, 2, 3, 5, and 10 wt% measured at 190°C.

(a) absolute magnitude of complex modulus ( $|G^*|$ ) as functions of applied frequency  
 (b)  $|G^*|$  at 0.1 rad/s and terminal slope as a function of clay concentration (solid lines represent fitted results (b)) (c) storage moduli ( $G'$ ) (d) loss moduli ( $G''$ ) at four representative angular frequencies (0.1, 1, 10, and 100 rad/s).



As shown in Figure 4.4.2 and 4.4.3, the size of the dispersed NR phase ( $D_n$ ,  $D_{vs}$ ) decreased as the amount of clay increased at below 3wt%. Although the clay contents increased further at above 3wt%, there was no significant change in the drop size of NR. These results match well the  $|G^*|$  at 0.1 rad/s and the slope of  $|G^*|$  at low frequency (Figure 4.4.1(b)). The change in location of the clay with the increasing clay content is traced with highly zoomed-in TEM images as shown in Figure 4.4.4. At lower clay concentrations, the clay is observed at the interface, while it starts to appear in PLA matrix when the concentration becomes higher. Especially at 10wt%, an obvious increase of clay in the matrix phase is observed. These results suggest that clay could work as an effective compatibilizer below a critical concentration. Thus, the size reduction of the dispersed phase is caused by the compatibilizing effect of the clay at the interface. In addition, the size distribution of the dispersed phase (polydispersity index, PI) is almost constant, suggesting a stable morphology of the dispersed phase, regardless of the clay content (Figure 4.4.3 and Table 4.4.1). According to the morphological observation, the nonterminal behavior of the PLA/NR blends in Figure 4.4.1 represents the increase in the total interfacial area between PLA and NR due to reduced drop size of the dispersed phase by compatibilizing effect of the clay added [13,41].

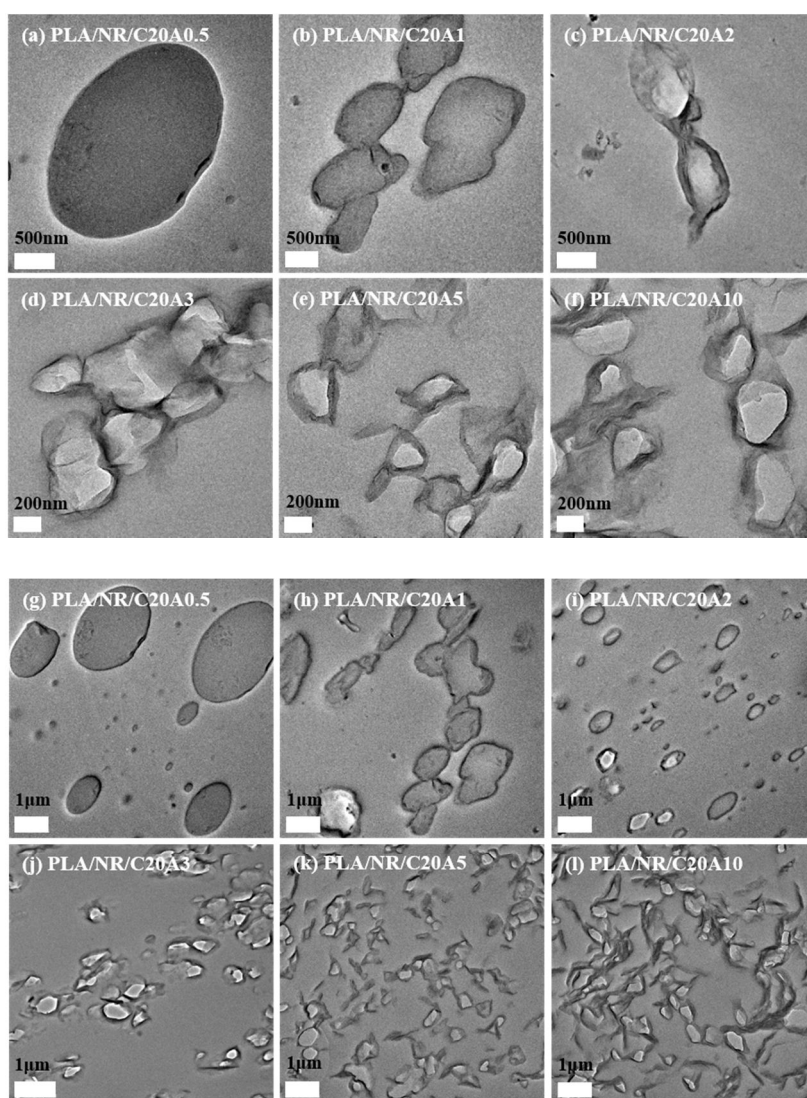


**Figure 4.4.2.** TEM images of PLA/NR blends with different C20A concentrations (0.5~10 wt%) with different magnification (scale bar is 500 nm for (a, b, c), 200 nm for (d, e, f) and 1 μm for (g, h, i, j, k, l).

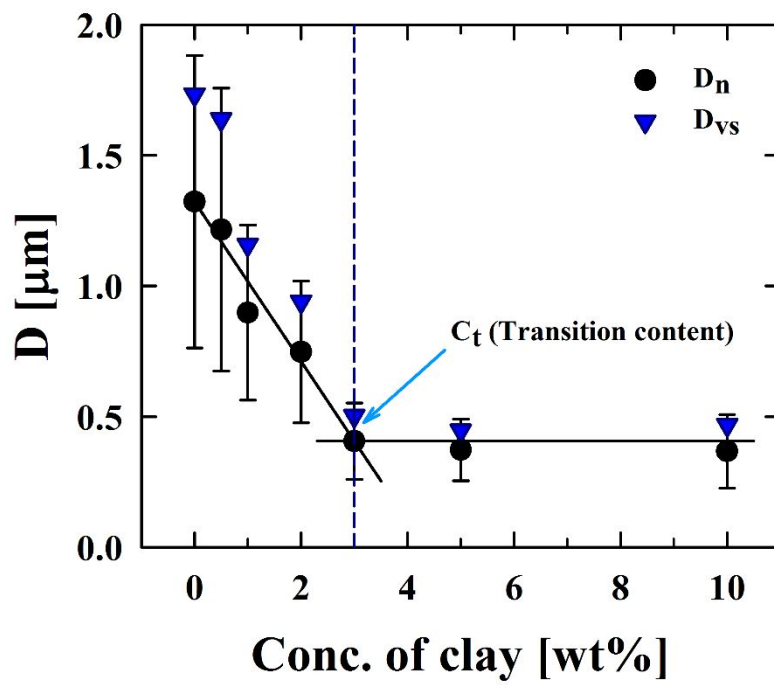


**Figure 4.4.3.** Drop size ( $D_n$ ,  $D_{vs}$ ) of the PLA/NR blends with different concentrations of C20A.

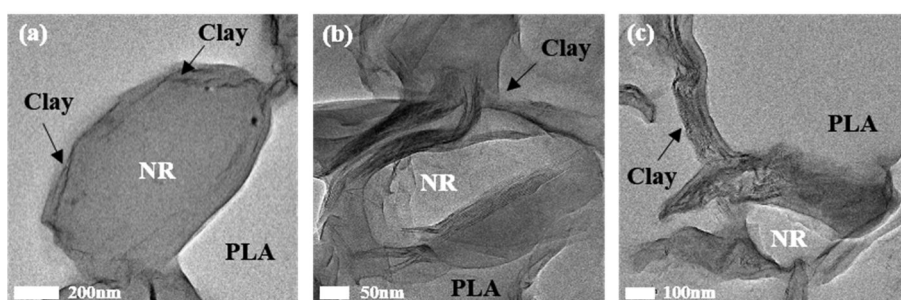


**Figure 4.4.4.** Highly zoomed-in TEM images for the PLA/NR blends with varied C20A contents (a) 1wt% (b) 3wt% (c) 5wt%.

**Table 4.4.1.**  $D_n$ ,  $D_{vs}$  and PI values of the PLA90/NR10 with various contents of C20A (0~10wt%).

C20A contents (wt%)	$D_n$ ( $\mu\text{m}$ )	$D_{vs}$ ( $\mu\text{m}$ )	PI [-]
0	$1.32 \pm 0.56$	1.73	1.31
0.5	$1.22 \pm 0.54$	1.64	1.35
1	$0.90 \pm 0.34$	1.16	1.29
2	$0.75 \pm 0.27$	0.94	1.26
3	$0.41 \pm 0.15$	0.50	1.24
5	$0.37 \pm 0.12$	0.45	1.20
10	$0.37 \pm 0.14$	0.47	1.28

The complex modulus of the blends with strain amplitude is shown in Figure 4.4.5. As the clay content increased, the  $|G^*|$  value increased. The difference in  $|G^*|$  according to the clay concentration is pronounced at a small strain amplitude region. Furthermore, the strain amplitude dependence of the complex moduli of the PLA/NR blends with higher concentrations of clay is enhanced, showing steep strain softening behavior. This result is influenced by the complex internal structure of the blends.

The nonlinear response can be analyzed more specifically by analyzing the raw stress data. Lissajous plot was introduced to analyze the structural development of materials qualitatively. Figure 4.4.6 depicts the elastic Lissajous loop (normalized stress ( $\sigma/\sigma_{\max}$ ) with the normalized strain ( $\gamma/\gamma_{\max}$ ) and the viscous loop (normalized stress ( $\sigma/\sigma_{\max}$ ) with the normalized strain rate ( $\dot{\gamma}/\dot{\gamma}_{\max}$ ). The elastic Lissajous loop of the PLA/NR blend displayed a circular shape, regardless of the strain amplitude (Figure 4.4.6(a)). However, in the case of PLA/NR/C20A, the elastic Lissajous pattern changed from a circular to an ellipsoidal shape as the concentration of clay increased. As shown in Figure 4.4.6(b), the viscous Lissajous loop followed a similar trend. The shape of the Lissajous curve of the PLA/NR does not change significantly, whereas that of PLA/NR/C20A varies with strain amplitude (See Figure 4.4.6(c) and (d), for example). These results imply that the inner structure of the blends becomes more complex due to the incorporated clay.

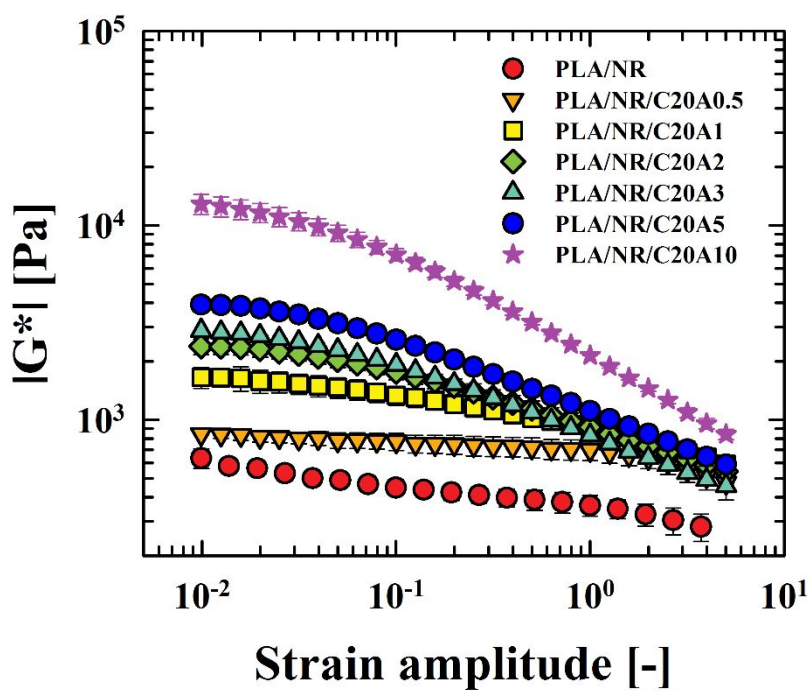


**Figure 4.4.5.**  $|G^*|$  of PLA/NR blends with different amounts of C20A (0–10 wt%) as a function of strain amplitude at 190°C.

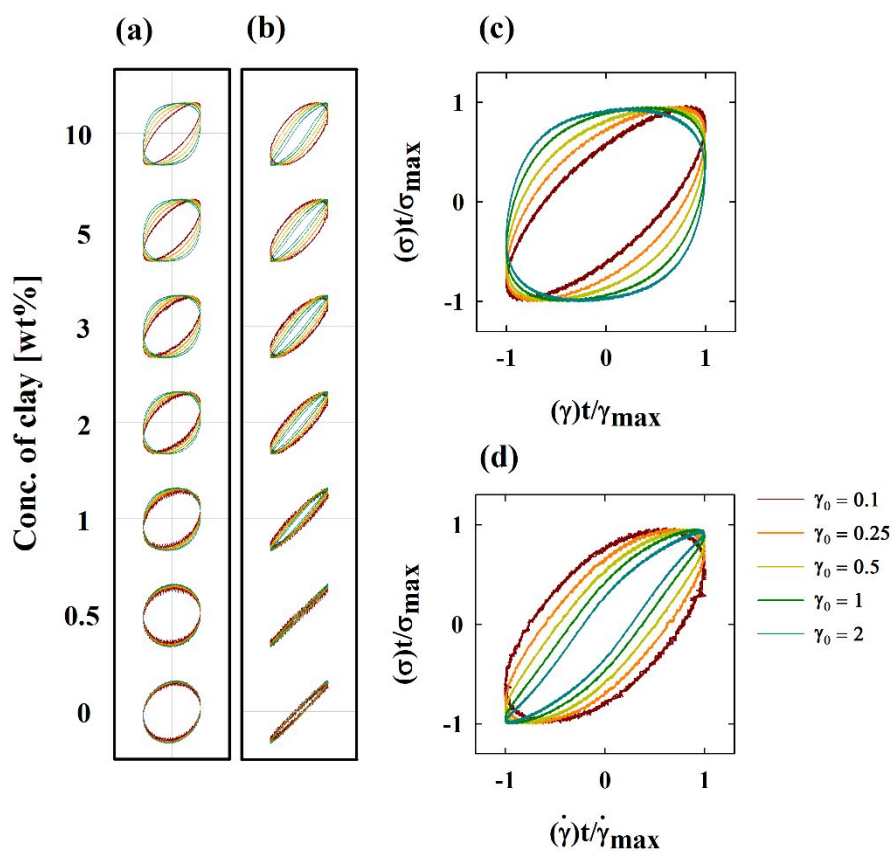


**Figure 4.4.6.** Normalized Lissajous pattern under fixed frequency (1 rad/s) and different strain amplitudes (0.1, 0.25, 0.5, 1, 2) of PLA/NR blends with the concentration of C20A. (a) Total stress vs. normalized strain, (b) total stress vs. normalized strain rate (c), (d) zoomed-in plot for  $\gamma/\gamma_{\max}$  vs  $\sigma/\sigma_{\max}$  and  $\dot{\gamma}/\dot{\gamma}_{\max}$  vs  $\sigma/\sigma_{\max}$  for blends with 10 wt% C20A, respectively.



FT-rheology is introduced to quantify the nonlinearity of the blends. Figure 4.4.7(a) exhibits a normalized third harmonic intensity ( $I_{3/1}$ ) value with the applied strain amplitude. The intensity of the PLA/NR blend increases with strain amplitude, showing a constant slope. In the case of PLA/NR/clay, the intensity increases up to the medium amplitude oscillatory shear (MAOS) region ( $\gamma_0 < 1$ ), then starts to decrease in the LAOS region ( $\gamma_0 > 1$ ). Additionally, the intensity of the PLA/NR/clay increases with clay contents. The increase in the  $I_{3/1}$  of the polymer blends is attributed to the interfacial tension reduction [52]. Hyun and Wilhelm [55] proposed a nonlinear coefficient,  $Q(\omega, \gamma_0) \equiv I_{3/1}/\gamma_0^2$ , as well as a zero-strain nonlinear coefficient,  $Q_0(\omega) \equiv \lim_{\gamma_0 \rightarrow 0} Q(\omega, \gamma_0)$ , which was proposed as an asymptotic value for the  $Q$  parameter from FT-rheology. A comparison of the calculated  $Q$  parameter of the blends with the fitting results obtained using a mathematical model [ $Q = Q_0 (1 + (C_1 \gamma_0)^{C_2})^{(C_3 - 1)/C_2}$ ] is shown in Figure 4.4.7(b). The results showed that zero-nonlinear coefficient ( $Q_0$ ), critical strain ( $\gamma_{oc} = 1/C_1$ ) and degree of strain thinning varied according to the concentration of clay (Table 4.4.2).

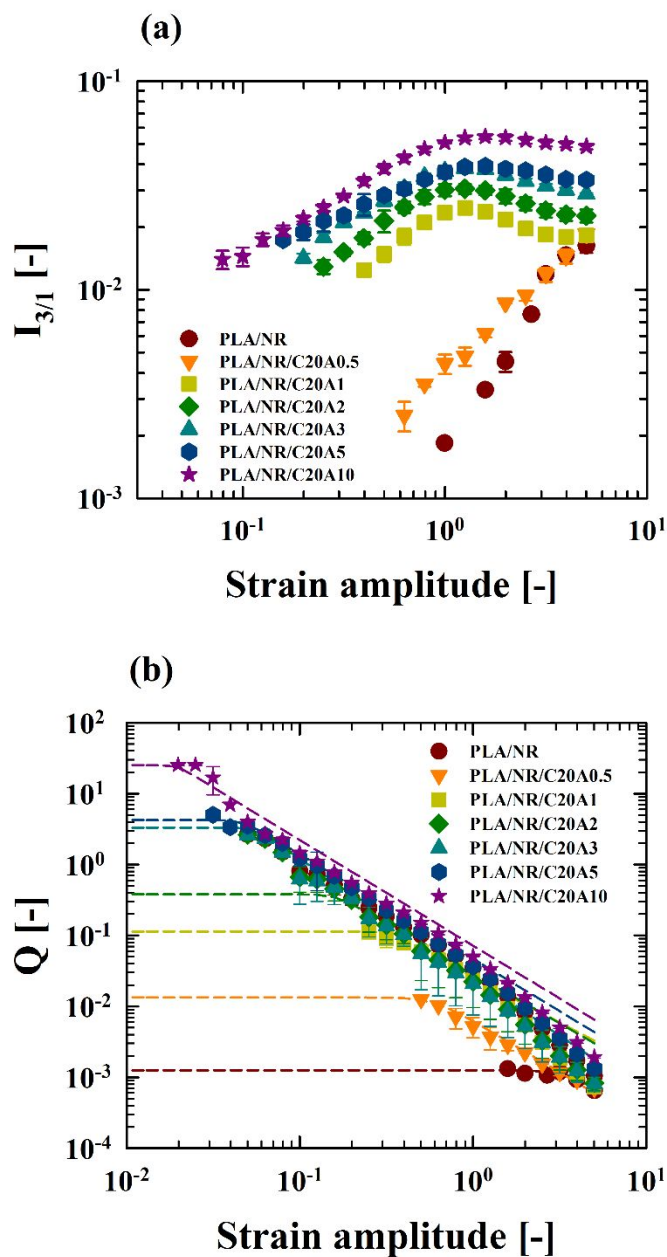


**Figure 4.4.7.** (a) Normalized third harmonic intensity ( $I_{3/1}$ ) from FT-rheology versus strain amplitude of the PLA/NR blends reinforced with various concentrations of C20A, (b) Nonlinearity  $Q$  of the blend with different contents of C20A with strain amplitude (symbol: experiments, line: fitting results).

**Table 4.4.2.** Fitting parameter of PLA/NR/C20A with different clay contents (0~10wt%).

Clay content (wt%)	$Q_0$	$C_1$	$C_2$	$C_3$
0	0.0125	0.22456	5.03986	-1.9735
0.5	0.01337	1.67841	5.67258	-0.4574
1	0.11321	3.17896	20.1318	-0.2778
2	0.38043	6.20247	9.18189	-0.4069
3	3.3010	18.3342	16.2250	-0.6620
5	4.24519	21.2510	10.8902	-0.4749
10	25.1534	51.1912	20.7524	-0.4887

The normalized zero-nonlinear coefficient ( $=Q_0(\varphi)/Q_0(0)$ ) and normalized complex moduli ( $=G^*(\varphi)/G^*(0)$ ) of PLA/NR/C20A are shown in Figure 4.4.8(a) and Table 4.4.3. The normalized  $|G^*|$  and normalized  $Q_0$  both increased as clay concentration increased. However, the normalized  $|G^*|$  gradually increased as the clay content was augmented, whereas the normalized  $Q_0$  showed transitional behavior at 3wt% of the clay, similar to SAOS results in Figure 4.4.1. Moreover, the rate of increase was faster for  $Q_0$  than  $|G^*|$ . These findings indicate that the nonlinearity of the blends is more sensitive than the linear viscoelasticity, which could be due to the complex internal structure of the blends. Lim et al. [58,59] proposed a NLR value (nonlinear-linear viscoelastic ratio, Eq. 4.4.1) that reflected the internal structure of complex fluids very sensitively:

$$NLR = \frac{Q_0(\varphi)/Q_0(0)}{|G^*(\varphi)|/|G^*(0)|} \quad (4.4.1)$$

where,  $\varphi$  is the filler concentration,  $Q_0$  is the asymptotic limiting and constant value of  $Q$  at low strain amplitude from LAOS tests, and  $|G^*|$  is the complex modulus from SAOS tests.

The NLR value of the PLA/NR blends is shown in Figure 4.4.8(b). The value increased sharply up to 3wt%, while it reached a plateau at higher concentrations of clay. The NLR value was previously related to the inverse droplet size of PP/PS blends [38,52]. The NLR value of the PLA/NR blend also represents the morphological change. The size of the dispersed phase decreases with the increase of

clay, and is approximately constant above 3wt% of the clay (Table 4.4.1). These findings correspond to the appearance of the plateau after an upturn in the NLR value (Figure 4.4.8(b)), suggesting that 3wt% is the optimum amount of clay that shows the highest compatibilization efficiency in the PLA/NR blends. Both the SAOS results ( $|G^*|$ ) and the LAOS results ( $Q_0$ ) only increase with increasing concentration of clay. However, the transition of NLR value was observed at 3 wt%, above which an almost plateau formed. NLR can give more exact information regarding drop size rather than only SAOS or LAOS results. These findings match the inverse of droplet size well, indicating that the NLR value is closely related to droplet information. Therefore, the NLR value was used to investigate the morphology under various experimental conditions.

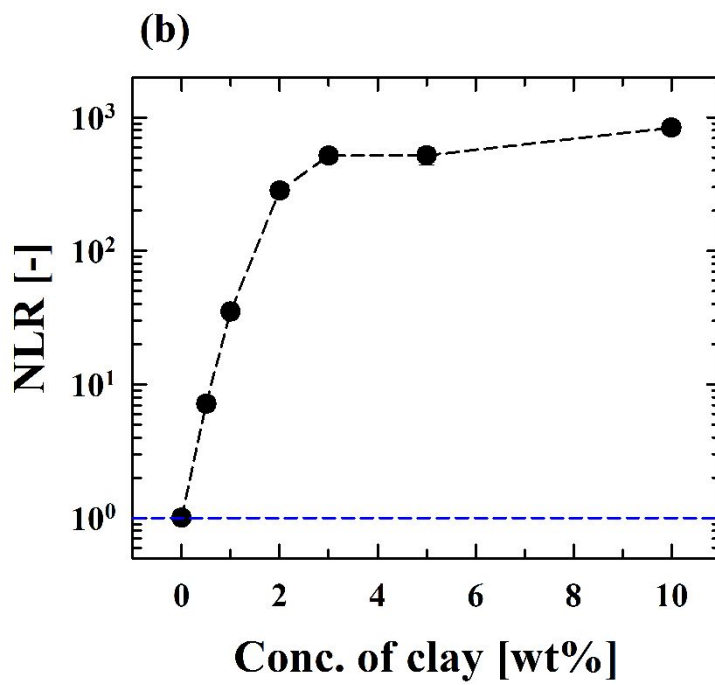
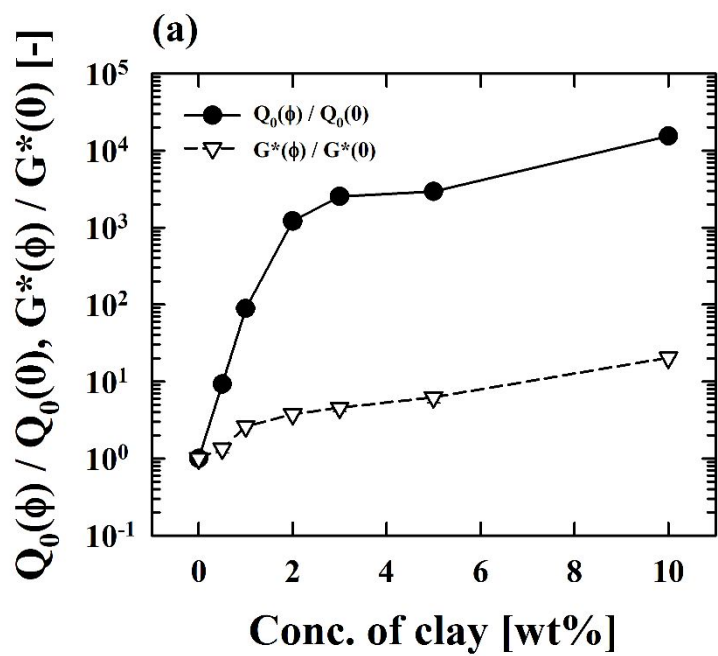


**Figure 4.4.8.** (a) Normalized  $Q_0$ , and normalized  $|G^*|$  (b) NLR value determined by Eq. 4.4.1 for PLA/NR/C20A blends.

**Table 4.4.3.**  $Q_0/Q_0(0)$ ,  $G^*/G^*(0)$  and NLR value of PLA90/NR10 blends with different concentration of C20A (0~10 wt%).

Samples	$Q_0/Q_0(0)$ [-]	$G^*/G^*(0)$ [-]	NLR [-]
PLA/NR/C20A0.5	9.26	1.34	7.12
PLA/NR/C20A1	88.92	2.60	35.0
PLA/NR/C20A2	1214.48	3.76	282
PLA/NR/C20A3	2645.63	4.56	516
PLA/NR/C20A5	3186.73	6.22	519
PLA/NR/C10A10	16966.89	20.27	837

#### **4.4.2. Mixing condition**

The structure and properties of polymer blends vary depending on processing conditions, such as compounding time, mixing rate or temperature. Mixing rate is especially important since it changes the capillary number which determines the breakup and coalescence of droplets of the dispersed phase. The effects of mixing rate on the PLA/NR/C20A3 blends were confirmed in comparison with the PLA/NR blend. The change in storage and loss moduli at 0.1 rad/s of the PLA/NR, as well as the PLA/NR/C20A3 blends prepared with different mixing rates (30, 50 and 100 rpm) are depicted in Figure 4.4.9. For the PLA/NR blend,  $G''$  was higher than that of  $G'$ , regardless of mixing rates.



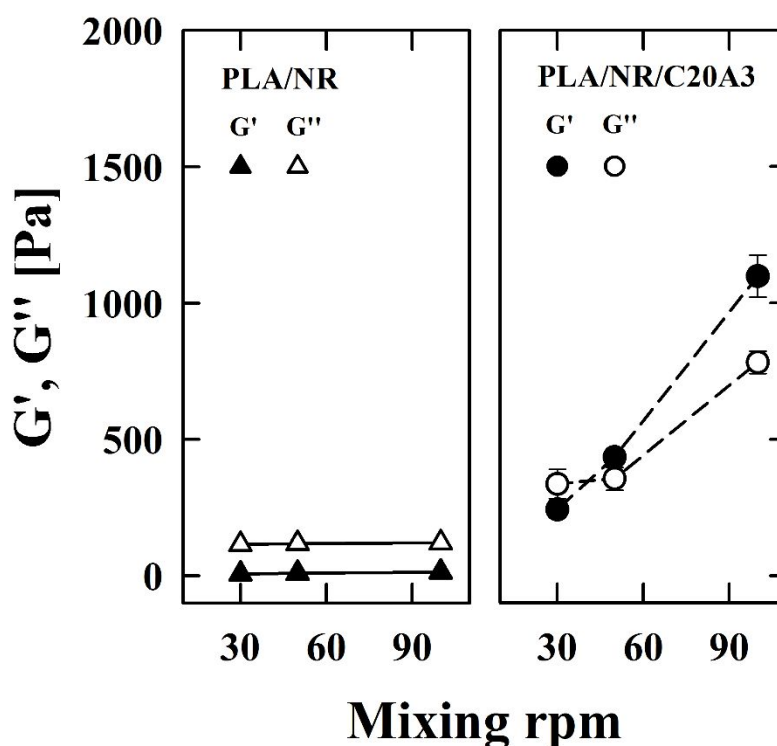


**Figure 4.4.9.**  $G'$ ,  $G''$  moduli of PLA/NR blends (left: without clay, right: with clay) measured at 0.1 rad/s 190°C. Clay (C20A) is added with 3wt%.

SEM revealed that there was no significant change in drop size or shape of the PLA/NR blend, regardless of the mixing rate (Figure 4.4.10(a)). In contrast, the  $G'$  and  $G''$  of the PLA/NR/C20A3 varied as mixing rates increased. For example, both moduli showed similar value at 30 rpm, and the  $G''$  became higher than  $G'$  at 50 and 100 rpm. Moreover, deformation of NR droplets was observed at 30 and 50 rpm, resulting in fibril morphology, and the drop changed to a nodular shape at 100 rpm. The drop size of PLA/NR/C20A3 decreased as mixing rpm increased (Figure 4.4.10(b) and (c)).

In immiscible polymer blends, the dispersed phase is known to be broken up only when a capillary number is higher than a critical capillary number at a given flow field (i.e., shear or extension flow). The drop size of the PLA/NR blend is not changed with the imposed mixing rate, since the capillary number does not reach the critical value, resulting in no significant change in rheological properties. Conversely, the change in drop size and rheological properties for PLA/NR/C20A3 suggest that the capillary number increased due to the incorporation of clay into the blend. The  $|G^*|$  and the  $Q_0$ , as well as the NLR values of the PLA/NR/C20A3 are listed in Table 4.4.4. The  $|G^*|$  at 100 rpm increased by approximately 1.41 times relative to that at 30 rpm, whereas the  $Q_0$  values showed a greater increase with increasing rpm. This change in  $Q_0$  value is attributed to the drop size reduction of the NR phase due to the clay, resulting in an increased NLR with mixing rates. Mixing at 100 rpm reduced the droplet size by 1.94 times ( $=0.97\mu\text{m}/0.50\mu\text{m}$ ) relative to mixing at 30 rpm. The trend for NLR with different mixing condition can also match the droplet size of the dispersed phase.

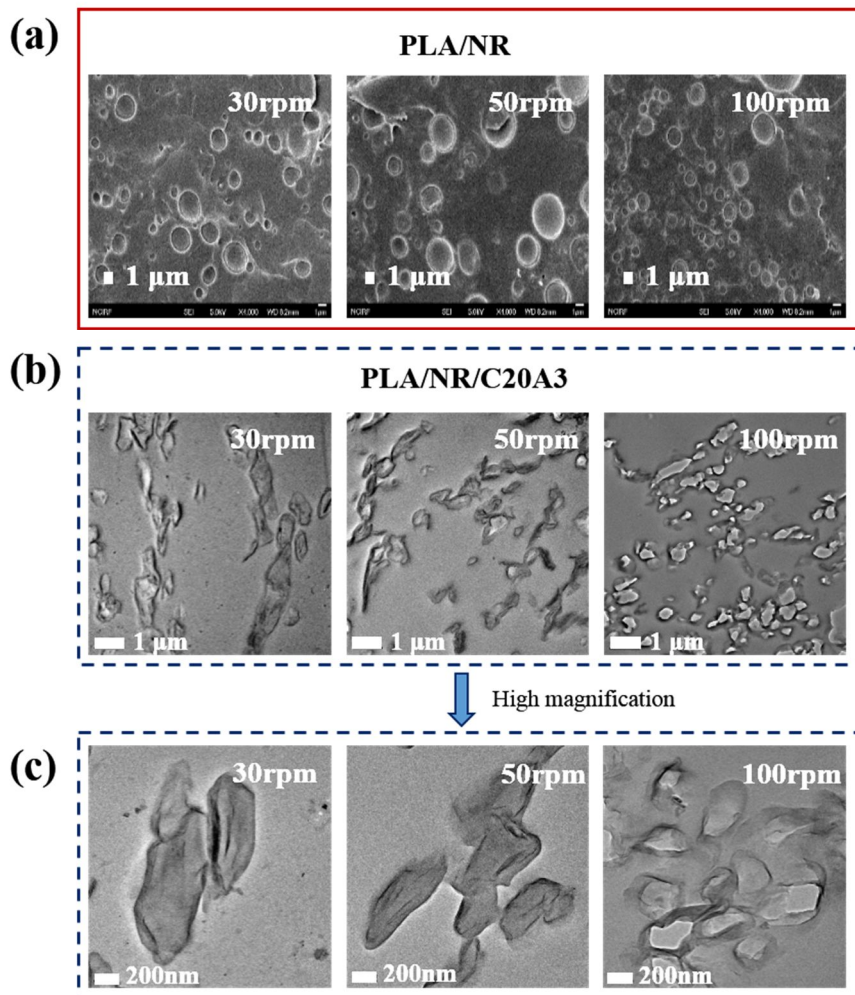


**Figure 4.4.10.** (a) SEM pictures of PLA/NR and (b), (c) TEM pictures of PLA/NR/C20A3 blends compounded at different mixing rpm (30, 50 and 100 rpm corresponding to approximated shear rate 14.1 23.6 and 47.1  $\text{s}^{-1}$ , respectively).

**Table 4.4.4.**  $Q_0$ ,  $|G^*|$ , NLR of PLA90/NR10/C20A3 blends with different mixing rpm (30, 50, 100).

RPM	$Q_0$ [-]	$ G^* $ [MPa]	NLR [-]
30	$0.56 \pm 0.03$	$2.01 \pm 0.04$	$118 \pm 5.93$
50	$0.74 \pm 0.01$	$2.17 \pm 0.03$	$144 \pm 3.07$
100	$3.39 \pm 0.13$	$2.54 \pm 0.15$	$485 \pm 28.1$

### 4.4.3. Types of clay

The compatibilizing effect of clay in the PLA/NR blend was investigated according to the types of clay. Three different types of clay (C10A, C20A, C30B) were introduced into the PLA/NR blend with fixed contents (3wt%). As shown in Figure 4.4.11(a),  $G''$  was higher than  $G'$  for the PLA/NR/C30B3 blend throughout the frequency range, while  $G'$  was higher than that of  $G''$  in the low frequency region for the PLA/NR/C20A3. In the case of PLA/NR/C10A3,  $G'$  was higher than  $G''$  at the broader frequency range. Moreover,  $G'$  and  $G''$  for PLA/NR/C10A3 showed a plateau in the low frequency domain, which represents a gel-like structure (Figure 4.4.11(b) and (c)). This change in moduli originated from the different compatibilization efficiency of each clay in the PLA/NR blends. Many previous studies have been conducted to determine reasons for different compatibilization efficiencies of clay with type. The efficiency was found to be changed with the selective location of clay due to differences in polarity, volume and viscosity between the matrix phase and dispersed phase. As previously mentioned, the selective location of the clay could be

estimated by calculating the wetting coefficient using Eq. 4.1.1. The clay would be located at the interface only when  $-1 < \omega_a < 1$ , otherwise it is entirely in the matrix phase or the dispersed phase. The wetting coefficient of three different clays calculated by the geometric mean approach is shown in Table 4.4.5 [34, 69-71].

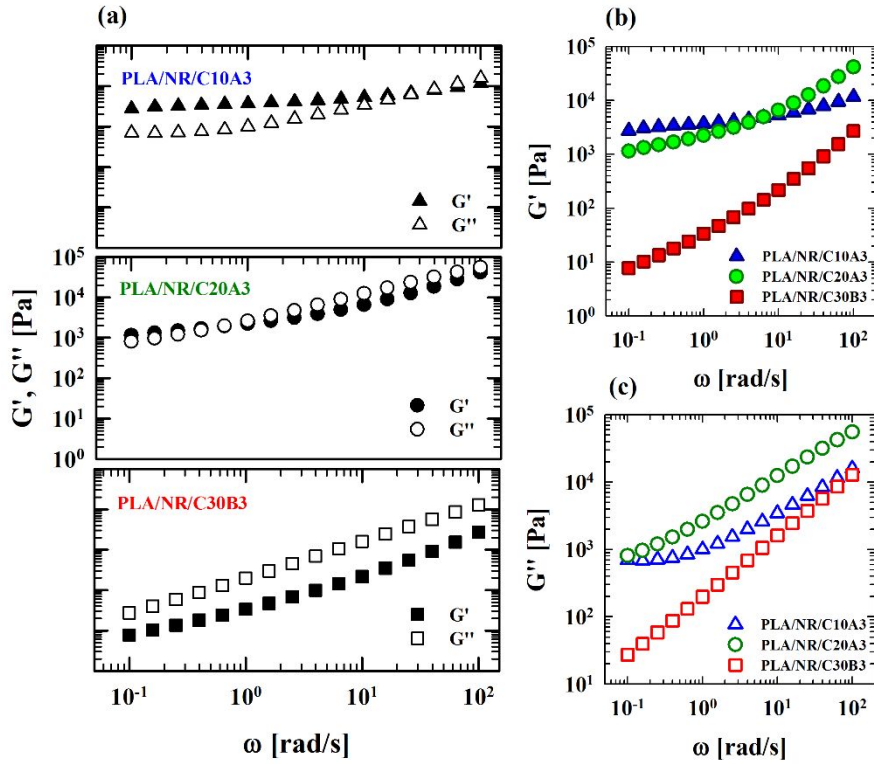


**Figure 4.4.11.** (a) Storage and loss moduli of PLA/NR/C10A3, PLA/NR/C20A3 and PLA/NR/C30B3 with angular frequencies ( $G'$  and  $G''$  are plotted separately in (b) and (c), respectively).

**Table 4.4.5.** Surface tension ( $\gamma$ ) and wetting coefficient ( $\omega_a$ ) of each material calculated by Eq. 4.1.1.

Material	$\gamma$ [mN·m <sup>-1</sup> ]	$\omega_a$ [-]
C10A	30.04	-0.9043
C20A	25.44	-0.3047
C30B	34.54	-1.4477

According to the wetting coefficient, C30B prefers being located in the matrix phase, while both C10A and C20A would be preferentially located at the interface. As shown in Figure 4.4.12, large agglomerates of C30B were observed in the matrix phase, whereas C10A and C20A were mainly located at the interface surrounding the dispersed phase. The position of each clay estimated by wettability is in agreement with the morphological observations. The drop size of NR decreased in the order of PLA/NR/C30B3 (0.75 $\mu$ m), PLA/NR/C20A3 (0.50 $\mu$ m) and PLA/NR/C10A3 (0.39 $\mu$ m). Taken together, these results clearly demonstrate that C10A is the most efficient compatibilizer, followed by C20A and C30B. These findings match the SAOS results well (Figure 4.4.11). Since C10A as well as C20A showed the same range of wettability ( $-1 < \omega_a < 1$ ), their compatibilization efficiency would be dependent on the nature of clay, such as its size, surfactant concentration and density. The density of organoclay could be considered a primary factor determining compatibilization efficiency. Due to its highly anisotropic structure, organoclay has a high excluded volume that restricts the motion of clay layers. The density difference between C10A (1.90 g/cm<sup>3</sup>) and C20A (1.77 g/cm<sup>3</sup>) results in the change in excluded volume

between those two clays. The larger surface of the dispersed phase could be enclosed by layers of C10A than that of C20A with the same weight fraction. Thus, the efficiency of C10A is higher than that of C20A, resulting in a smaller drop size of PLA/NR/C10A3 than the blend with C20A.

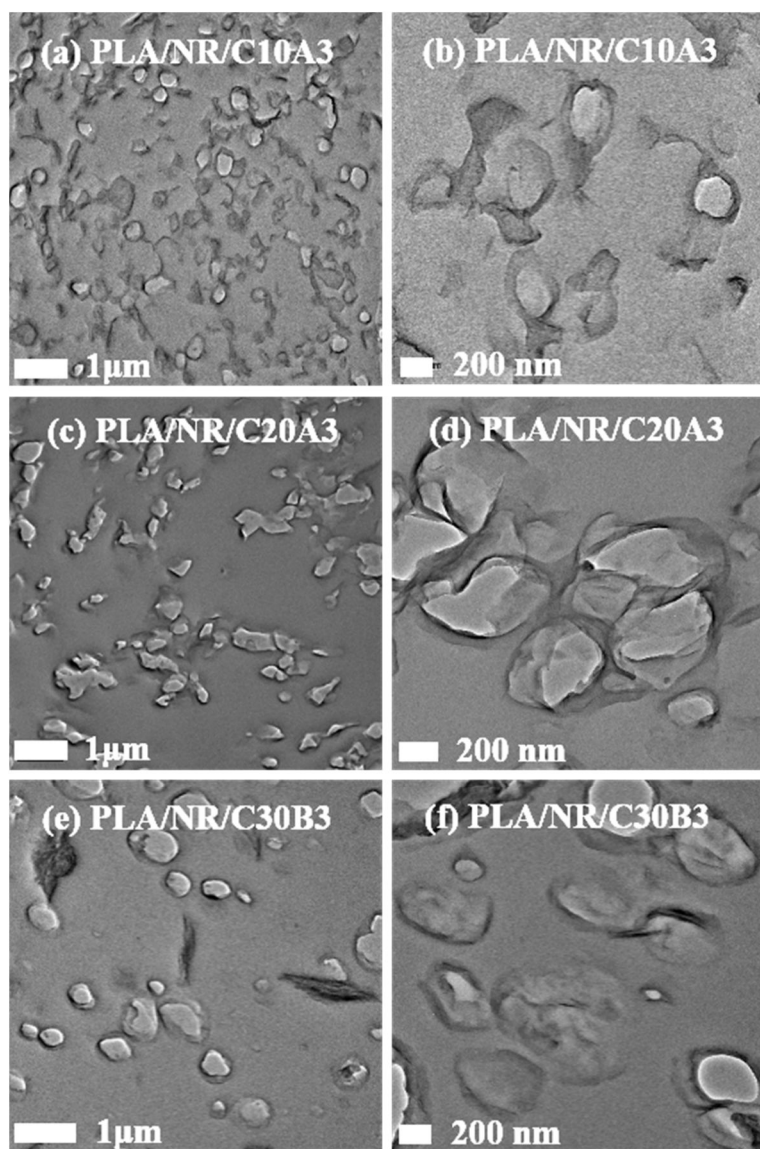


**Figure 4.4.12.** TEM images of PLA/NR blends filled with different types of clays (3wt%). (a), (b) C10A, (c), (d) C20A, (e), (f) C30B.



The linear viscoelasticity and the nonlinearity of each PLA/NR/clay are displayed in Figure 4.4.13. The  $I_{3/1}$  value with the strain amplitude increased in the order of PLA/NR/C30B3, PLA/NR/C20A3 and PLA/NR/C10A3, as did the normalized  $Q_0$ . The rate of increase in the normalized  $Q_0$  was more rapid than that of the normalized  $|G^*|$  value. These findings again clearly demonstrate that the nonlinearity is more sensitive than the linear viscoelastic  $|G^*|$  value for describing the change in the inner structure of polymer blend systems, similar to the effects of mixing condition on rheological properties. As depicted in Figure 4.4.14 and Table 4.4.6, the NLR showed the greatest increase for PLA/NR/C10A3, followed by PLA/NR/C20A3 and PLA/NR/C30B3. The averaged drop size of the dispersed phase decreased in the order of PLA/NR/C30B, PLA/NR/C20A and PLA/NR/C10A. The NLR value match the change in drop size of each blend well.

Accordingly, NLR is found to be correlated with the inverse of the drop size of the PLA/NR blends for each parameter in this work (concentration of clay, mixing condition, and types of clay).

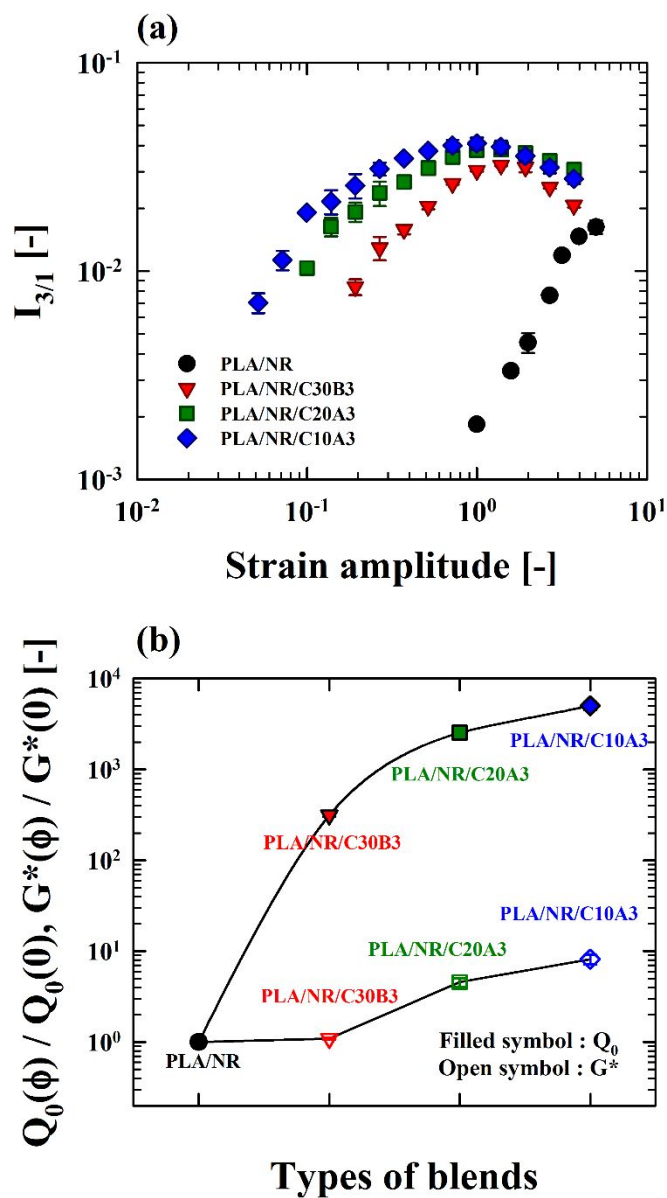


**Figure 4.4.13.** (a)  $I_{3/1}$  as a function of strain amplitude, (b) comparison between  $[Q_0(\phi)/Q_0]$  and  $[G^*(\phi)/G^*(0)]$  for each blends (PLA/NR, PLA/NR/C30B3, PLA/NR/C20A3 and PLA/NR/C10A3). All clay (C30B, C20A, C10A) is added 3wt% on PLA/NR blends.

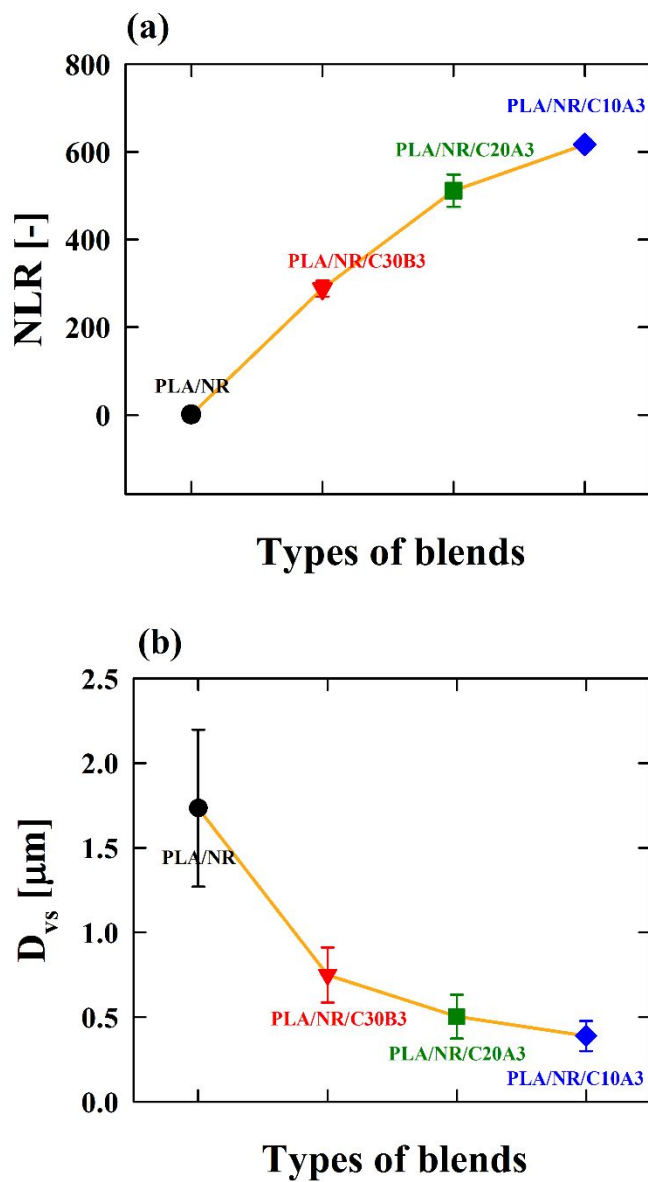


**Figure 4.4.14.** (a) NLR value and (b) inverse volume-to-surface averaged drop diameter ( $1/D_{vs}$ ) of PLA/NR blends with 3wt% of different types of clay (C10A, C20A, C30B).

**Table 4.4.6.** List of  $Q_0/Q_0(0)$ ,  $G^*/G^*(0)$  and NLR value of PLA90/NR10 blends with 3wt% of different types of clay (C10A, C20A, C30B) measured 1 rad/s at 190°C.

Samples	$Q_0/Q_0(0)$ [-]	$G^*/G^*(0)$ [-]	NLR [-]
PLA/NR/C30B3	$322.4 \pm 12.1$	$1.09 \pm 0.03$	$288 \pm 18.1$
PLA/NR/C20A3	$2538 \pm 151$	$4.57 \pm 0.51$	$489.5 \pm 6.38$
PLA/NR/C10A3	$5030 \pm 528$	$8.12 \pm 1.01$	$625.1 \pm 11.9$

#### 4.4.4. Relation between NLR and drop diameter

The relationship between the NLR and inverse of drop size is depicted in Figure 4.4.15. The inverse of drop diameter approximately increased linearly with increasing NLR value for all cases (Figure 4.4.15(a)). Thus, an empirical relationship between those two parameters is suggested:  $NLR = a / D_{vs} + b$ . Some data points show deviation from the linear plot ( $R^2=0.8625$ ) and the NLR at the 10wt% of C20A content highly diverges from linear relation. These deviations might be attributed to size distribution of droplets and increased interaction between PLA and C20A due to effect of clay as a reinforcing filler in the matrix phase (Figure 4.4.2(I)). These results suggest that drop size could be approximately estimated for the PLA/NR/clay system when the NLR value is obtained. When the relation between the NLR and the inverse of drop diameter is observed within linear-log scale (Figure 4.4.15(b)), the NLR value seems to reach a certain saturated level with the decrease of drop diameter. Thus, the trend for NLR in wider range of drop diameter needs to be examined as a follow up work. Additionally, slope 'a' and intercept 'b' might be determined by the nature of the matrix polymer and the dispersed polymer. The details regarding this empirical equation and the physical meaning of each parameter should be investigated further using a theoretical model.

Overall, a strategy in which the NLR value can be applied to characterize the PLA/NR blend compatibilized by the organoclays was developed. The importance of NLR value as a characterization tool to detect morphological development of polymer blends was verified by this study.

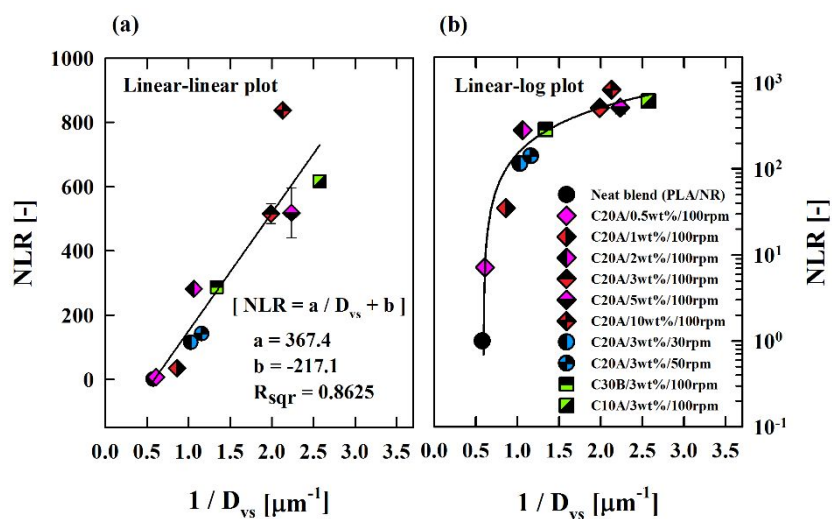


**Figure 4.4.15.**  $1/D_{vs}$  vs. NLR (solid line represents fitted results). (a) linear-linear plot and (b) linear-log plot.

# **Chapter 5.**

## **Conclusion**

In this thesis, the role of organoclay as a compatibilizer when added to an immiscible PLA/NR blend system was investigated. The blends exhibited a different morphological and physical properties depending on the location and contents of the clay. Below the critical amount (3wt%), the clay acted as an effective compatibilizer. All the clays were localized at the interface (or dispersed phase) reducing the interfacial tension and decreasing the drop size of NR. In contrast, when an excess amount above 3wt% was added, the clays appeared in the matrix phase as well. In addition, the size of the dispersed phase was almost constant. Analysis of the rheological properties – especially the increase of the modulus in the terminal region – revealed that the blend formed a strong network with the addition of the clay. When a clay content of 2~3wt% was incorporated, the blend showed strong strain hardening behavior. However, the strain hardening behavior disappeared at higher clay contents. This trend was similar to the trend of the mechanical properties. When the clay existed only at the interface, the elongation at break increased due to the clay as a compatibilizer, while the tensile strength showed a significant reduction. At concentrations higher than 3wt%, where the clay was also present in the PLA phase, the elongation at break was significantly decreased. In conclusion, it is possible to improve the performance of a polymer blend system by localizing clay at the interface with an appropriate material composition.

Next, the nonlinear viscoelastic properties of poly(lactic acid) (PLA) and natural rubber (NR) blends compatibilized with organoclay according to clay contents, mixing conditions and types of clay were examined. The drop size of the dispersed phase decreased with increasing clay (C20A) concentration up to 3wt%, above which



it became constant. Nonlinearity ( $I_{3/1}$ ) reflected the internal structure of the blends more sensitively than the linear viscoelastic properties. The nonlinear-linear viscoelastic ratio (NLR) represented the change in drop size of NR according to the C20A concentration. The effects of mixing rates were also examined via linear and nonlinear rheological analysis. As mixing rate increased, the drop deformed and its size decreased, whereas the morphology of the PLA/NR blend did not change significantly under the same conditions. The NLR value of PLA/NR/C20A according to mixing rates represented the reduction in drop size well. The effects of types of clay (C10A, C20A, C30B) for structure and property changes in the PLA/NR blends were also investigated. The drop size of the dispersed phase decreased most with C10A, followed by C20A and C30B, corresponding to the compatibilization efficiency. The NLR value displayed a similar trend as the drop size reduction and was related to the inverse of the drop size for all variables (clay concentration, mixing condition and types of clay). Taken together, these results demonstrated that the NLR value could be used to estimate the compatibilizing effect of organoclay in immiscible polymer blends. The correlation between NLR value and drop size of the dispersed phase in polymer blends was clearly demonstrated in this study.

## References

1. Taylor, G.I. Proc. R. Soc. London Ser. A **1934**, 146, 501-523.
2. Fornes, T.D.; Yoon, P.J.; Hunter, D.L.; Keskkula, H.; Paul, D.R. Effect of organoclay structure on nylon 6 nanocomposite morphology and properties. *Polymer* **2002**, 43, 5915-5933.
3. Cai, D.; Song, M. Ultra-high enhancement in the toughness of polyethylene by exfoliated natural clay nanosheets. *J. Appl. Polym. Sci.* **2015**, 132, 41314.
4. Lee, H.-S.; Fasulo, P.D.; Rodgers, W.R.; Paul, D.R. TPO based nanocomposites. Part 2. Thermal expansion behavior. *Polymer* **2006**, 47, 3528-3539.
5. Kim, D.H.; Fasulo, P.D.; Rodgers, W.R.; Paul, D.R. Effect of the ratio of maleated polypropylene to organoclay on the structure and properties of TPO-based nanocomposites. Part II: Thermal expansion behavior. *Polymer* **2008**, 49, 2492-2506.
6. Kiliaris, P.; Papaspyrides, C.D. Polymer/layered silicate (clay) nanocomposites: An overview of flame retardancy. *Prog. Polym. Sci.* **2010**, 35, 902-958.
7. Yi, d.; Yang, R.; Wilkie, C.A. Full scale nanocomposites: Clay in fire retardant and polymer. *Polym. Degrad. Stab.* **2014**, 105, 31-41.

8. Bharadwaj, R.K. Modeling the barrier properties of polymer-layered silicate nanocomposites. *Macromolecules* **2001**, 34, 9189-9192.
9. Choudalakis, G.A.; Kalo, H. Breu, J. Gotsis, A.D. CO<sub>2</sub> gas barrier properties in polymer nanocomposite coatings containing Li-Hecorite clays. *J. Appl. Polym. Sci.* **2014**, 131, 40805.
10. Fukushima, K.; Abbate, C.; Tabuani, D.; Gennari, M.; Camino, G. Biodegradation of poly(lactic acid) and its nanocomposites. *Polym. Degrad. Stab.* **2009**, 94, 1646-1655.
11. Mantia, F.P.L.; Arrigo, R.; Morreale, M. Effect of the orientation and rheological behaviour of biodegradable polymer nanocomposites. *Eur. Polym. J.* **2014**, 54, 11-17.
12. Ock, H.G.; Ahn, K.H.; Lee, S.J.; Effect of electric field on polymer/clay nanocomposites depending on the affinities between the polymer and clay. *J. Appl. Polym. Sci.* **2016**, DOI: 10.1002/app.43582.
13. Hong, J.S.; Han, N.; Ahn, K.H.; Lee, S.J.; Kim, C. The role of organically modified layered silicate in the breakup and coalescence of droplets in PBT/PE blends. *Polymer* **2006**, 47, 3967-3975.
14. Hong, J.S.; Kim, Y.K.; Ahn, K.H.; Lee, S.J.; Kim, C. Interfacial tension reduction in PBT/PE/Clay nanocomposite. *Rheol. Acta* **2007**, 46, 469-478.

15. Linnemann, B.; Sri Harwoko, M.; Gries, T. Polylactide fibers (PLA). *Chem. Fibers Int.* **2003**, 53, 426-433.
16. Rasal, R.M.; Janorkar A.V.; Hirt, D.E. Poly(lactic acid) Modification. *Prog. Polym. Sci.* **2010**, 35, 338-356.
17. Drumright, R.E.; Gruber, P.R.; Henton, D.E. Polylactic acid technology. *Adv Mater.* **2000**, 12, 1841-1846.
18. Dorgan, J.R.; Lehermeier, H.; Mang, M. Thermal and rheological properties of commercial-grade poly(lactic acid)s. *J. Polym. Environ.* **2000**, 8, 1-9.
19. Nampoothiri, K.M.; Nair, N.R.; John, R.P. An overview of the recent development in polylactide (PLA) research. *Bioresour. Technol.* **2010**, 101, 8493-8501.
20. Li, Y.; Shimizu, H. Toughening of Polylactid by Melt Blending with a Biodegradable Poly(ether)urethane Elastomer. *Macromol. Biosci.* **2007**, 7, 921-928.
21. Hassouna, F.; Raquez, J.-M.; Addiego, F.; Toniazzo, V.; Dubois, P.; Ruch, D. New development on plasticized poly(lactide): Chemical grafting of citrate on PLA by reactive extrusion. *Eur. Polym. J.* **2012**, 48, 404-415.
22. Choi, K.-m.; Choi, M.-C.; Han, D.-H.; Park, T.-S.; Ha, C.-S. Plasticization of poly(lactic acid) (PLA) through chemical grafting of poly(ethylene glycol)

- (PEG) via in situ reactive blending. *Eur. Polym. J.* **2013**, 49, 2356-2364.
23. Bitinis, N.; Verdejo, R.; Cassagnau, P.; Lopez-Manchado, M.A. Structure and properties of polylactide/natural rubber blends. *Mater. Chem. Phys.* **2011**, 129, 823-831.
  24. Huang, Y.; Zhang, C.; Pan, Y.; Zhou, Y.; Jiang L.; Dan, Y. Effect of NR on the hydrolytic degradation of PLA. *Polym. Degrad. Stab.* **2013**, 98, 943-950.
  25. Ishida, S.; Nagasaki, R.; Chino, K.; Dong, T.; Inoue, Y. Toughening of poly(L-lactide) by melt blending with rubbers. *J. Appl. Polym. Sci.* **2009**, 113, 558-566.
  26. Jaratrotkamjorn, R.; Khaokong, C.; Tanrattanakul, V. Toughness enhancement of poly(lactic acid) by melt blending with natural rubber. *J. Appl. Polym. Sci.* **2012**, 124, 5027-5036.
  27. Rose, K.; Steinbüchel, A. Biodegradation of natural rubber and related compounds: Recent insights into a hardly understood catabolic capability of microorganisms. *Appl. Environ. Microbiol.* **2005**, 71, 2803-2812.
  28. Lyu, S.; Jones, T.D.; Bates, F.S.; Macosko, C.W. Role of block copolymers on suppression of droplet coalescence. *Macromolecules* **2002**, 35, 7845-7855.
  29. Chow, W.S.; Ishak, Z.A.M.; Karger-Kocsis, J.; Apostolov, A.A.; Ishiaku, U.S. Compatibilizing effect of maleated polypropylene on the mechanical properties

- and morphology of injection molded polyamide 6/polypropylene/organoclay nanocomposites. *Polymer* **2003**, 44, 7427-7440.
30. Menyhárd, A.; Varga, J. The effect of compatibilizers on the crystallization, melting and polymorphic composition of  $\beta$ -nucleated isotactic polypropylene and polyamide 6 blends. *Eur. Polym. J.* **2006**, 42, 3257-3268.
31. Lai, S.-M.; Li, H.-C.; Liao, Y.-C. Properties and preparation of compatibilized nylon 6 nanocomposites/ABS blends: Part II -Physical and thermal properties. *Eur. Polym. J.* **2007**, 43, 1660-1671.
32. Deleo, C.L.; Velankar, S.S. Morphology and rheology of compatibilized polymer blends: Diblock compatibilizers vs crosslinked reactive compatibilizers. *J. Rheol.* **2008**, 52, 1385-1404.
33. Zhang, Z.L.; Zhang, H.D.; Yang, Y.L.; Vinckier, I.; Luan, H.M. Rheology and morphology of phase-separating polymer blends. *Macromolecules* **2001**, 34, 1416-1429.
34. Bitinis, N.; Verdejo, R.; Maya, E.M.; Espuche, E.; Cassagnau, P.; Lopez-Manchado, M.A. Physicochemical properties of organoclay filled polylactic acid/natural rubber blend bionanocomposites. *Compos. Sci. Technol.* **2012**, 72, 305-313.
35. Bitinis, N.; Sanz, A.; Nogales, A.; Verdejo, R.; Lopez-Manchado, M.A.;

- Ezquerro, T.A. Deformation mechanisms in polylactic acid/natural rubber/organoclay bionanocomposites as revealed by synchrotron X-ray scattering. *Soft Matter* **2012**, 8, 8990-8997.
36. Elias, L.; Fenouillot, F.; Majeste, J.C.; Cassagnau, P. Morphology and rheology of immiscible polymer blends filled with silica nanoparticles. *Polymer* **2007**, 48, 6029-6040.
37. Hong, J.S.; Hong, I.G.; Lim, H.T.; Ahn, K.H.; Lee, S.J. In situ lubrication dispersion of multi-walled carbon nanotubes in poly(propylene) melts. *Macromol. Mater. Eng.* **2012**, 297, 279-287.
38. Salehiyan, R.; Song, H.Y.; Choi, W.J.; Hyun, K. Characterization of effect of silica nanoparticles on (80/20) PP/PS blends via nonlinear rheological properties from Fourier transform rheology. *Macromolecules* **2015**, 48, 4669-4679.
39. Park, J.; Lee, S.; Lee J.W. Effect of manufacturing condition in PC/PMMA/CNT nanocomposites extrusion on the electrical, morphological, and mechanical properties. *Korea-Aust. Rheol. J.* **2015**, 27, 55-62.
40. Forouharshad, M.; Gardella, L.; Furfaro, D.; Galimberti, M.; Monticelli, O. A low-environmental-impact approach for novel bio-composites based on PLLA/PCL blends and high surface area graphite. *Eur. Polym. J.* **2015**, 70, 28-36.

41. Ray, S.S.; Pouliot, S.; Bousmina, M.; Utracki, L.A. Role of organically modified layered silicate as an active interfacial modifier in immiscible polystyrene/polypropylene blends. *Polymer* **2004**, *45*, 8403-8413.
42. Kim, H.B.; Choi, J.S.; Lee, C.H.; Lim, S.T.; Jhon, M.S.; Choi, H.J. Polymer blend/organoclay nanocomposites with poly(ethylene oxide) and poly(methyl methacrylate). *Eur. Polym. J.* **2005**, *41*, 679-685.
43. Hong, J.S.; Han, N.; Ahn, K.H.; Lee, S.J.; Kim, C. The role of organically modified layered silicate in the breakup and coalescence of droplets in PBT/PE blends. *Polymer* **2006**, *47*, 3967-3975.
44. Hong, J.S.; Kim, Y.K.; Ahn, K.H.; Lee, S.J.; Kim, C. Interfacial tension reduction in PBT/PE/Clay nanocomposite. *Rheol. Acta* **2007**, *46*, 469-478.
45. Gcwabaza, T.; Ray, S.S.; Focke, W.W.; Maity, A. Morphology and properties of nanostructured materials based on polypropylene/poly(butylene succinate) blend and organoclay. *Eur. Polym. J.* **2009**, *45*, 353-367.
46. Cho, S.; Hong, J.S.; Lee, S.J.; Ahn, K.H.; Covas, J.A.; Maia, J.M. Morphology and rheology of polypropylene/polystyrene/clay nanocomposites in batch and continuous melt mixing processes. *Macromol. Mater. Eng.* **2011**, *296*, 341-348.
47. Bijarimi, M.; Ahmad, S.; Rasid, R. Mechanical, thermal and morphological properties of poly(lactic acid)/natural rubber nanocomposites. *J. Reinf. Plast.*



- Compos. **2013**, 32, 1656-1667.
48. Larson, R.G. The structure and rheology of complex fluids: New York, **1999**.
49. Solomon, M.J.; Almusallam, A.S.; Seefeldt, K.F.; Somwangthanaroj, A.; Varadan, P. Rheology of polypropylene/clay hybrid materials. *Macromolecules* **2001**, 34, 1864-1872.
50. Hong, J.S.; Kim, Y.K.; Ahn, K.H.; Lee, S.J. Shear-induced migration of nanoclay during morphology evolution of PBT/PS blend. *J. Appl. Polym. Sci.* **2008**, 108, 565-575.
51. Palierne, J.F. Linear rheology of viscoelastic emulsion with interfacial tension. *Rheol. Acta* **1990**, 29, 204-214.
52. Salehiyan, R.; Yoo, Y.; Choi, W.J.; Hyun, K. Characterization of morphologies of compatibilized polypropylene/polystyrene blends with nanoparticles via nonlinear rheological properties from FT-Rheology. *Macromolecules* **2014**, 47, 4066-4076.
53. Hyun, K.; Kim, S.H.; Ahn, K.H.; Lee, S.J. Large amplitude oscillatory shear as a way to classify the complex fluids. *J. Non-Newtonian Fluid Mech.* **2001**, 107, 51-65.
54. Carotenuto, C.; Grosso, M.; Maffettone, P.L. Fourier transform rheology of dilute immiscible polymer blends: A novel procedure to probe blend

- morphology. *Macromolecules* **2008**, 41, 4492-4500.
55. Hyun, K.; Wilhelm, M.; Establishing a new mechanical nonlinear coefficient  $Q$  from FT-rheology: First investigation of entangled linear and comb polymer model systems. *Macromolecules* **2009**, 42, 411-422.
56. Reinheimer, K.; Grosso, M.; Wilhelm, M. Fourier transform rheology as a universal non-linear mechanical characterization of droplet size and interfacial tension of dilute monodisperse emulsions. *J. Colloid Interface Sci.* **2011**, 360, 818-825.
57. Hyun, K.; Wilhelm, M.; O. Klein, C.; Cho, K. S.; Nam, J. G.; Ahn, K. H.; Lee, S. J.; Ewoldt, R. H.; McKinley, G. H. A review of nonlinear oscillatory shear tests: Analysis and application of large amplitude oscillatory shear (LAOS). *Prog. Polym. Sci.* **2011**, 36, 1697-1753.
58. Hyun, K.; Lim, H.T.; Ahn, K.H. Nonlinear response of polypropylene (PP)/clay nanocomposites under dynamic oscillatory shear flow. *Korea-Aust. Rheol. J.* **2012**, 24 (2), 113-120.
59. Lim, H. T.; Ahn, K. H.; Hong, J. S.; Hyun, K. Nonlinear viscoelasticity of polymer nanocomposites under large amplitude oscillatory shear flow. *J. Rheol.* **2013**, 57, 767-789.
60. Salehiyan, R.; Hyun, K.; Effect of organoclay on non-linear rheological

- properties of poly(lactic acid)/poly(caprolactone) blends. *Korean J. Chem. Eng.* **2013**, 30, 1013-1022.
61. Wilhelm, M.; Maring, D.; Spiess, H. W. Fourier-transform rheology. *Rheol. Acta* **1998**, 37 (4), 399–405.
62. Wilhelm, M.; Reinheimer, P.; Ortseifer, M. High sensitivity Fourier-transform rheology. *Rheol. Acta* **1999**, 38 (4), 349–356.
63. Wilhelm, M.; Reinheimer, P.; Ortseifer, M.; Neidhöfer, T.; Spiess, H. W. The crossover between linear and non-linear mechanical behavior in polymer solutions as detected by Fourier-transform rheology. *Rheol. Acta* **2000**, 39, 241–246.
64. Kyu, H. Analysis and application of nonlinear rheological properties by large amplitude oscillatory shear (LAOS) test. *Polymer Science and Technology* **2013**, 24, 183-190.
65. Ock, H.G.; Kim, D.H.; Ahn, K.H.; Lee, S.J.; Maia, J.M. Effect of Organoclay as a Compatibilizer in Poly(lactic acid) and Natural Rubber Blends. *Eur. Polym. J.* **2016**, 76, 216-227.
66. Ock, H.G.; Ahn, K.H.; Lee, S.J.; Kyu, H. Characterization of compatibilizing effect of organoclay in poly(lactic acid) and natural rubber blends by FT-rheology. *Macromolecules* **2016**, 49, 2832-2842.

67. Marić, M.; Macosko, C.W. Improving polymer blend dispersions in mini-mixers. *Polym. Eng. Sci.* **2001**, 41, 118-130.
68. Pogodina, N.V.; Cerclé C.; Avérous, L.; Thomann, R.; Bouquey, M.; Muller, R. Processing and characterization of biodegradable polymer nanocomposites: Detection of dispersion state. *Rheol. Acta* **2008**, 47, 543-553.
69. Ho, C.C.; Khew, M.C. Surface free energy analysis of natural and modified natural rubber latex films by contact angle method. *Langmuir* **2000**, 16, 1407-1414.
70. Biresaw, G.; Carriere, C.J. Correlation between mechanical adhesion and interfacial properties of starch/biodegradable polyester blends. *J. Polym. Sci., Part B: Polym. Phys.* **2001**, 39, 920-930.
71. Ellias, L.; Fenouillot, F.; Majesté, J.C., Martin, G.; Cassagnau, P. J. Migration of nanosilica particles in polymer blends. *Polym. Sci., Part B: Polym. Phys.* **2008**, 46, 1976-1983.
72. Solomon, M.J.; Almusallam, A.S.; Seefeldt, K.F.; Somwangthanaroj, A.; Varadan, P. Rheology of polypropylene/clay hybrid materials. *Macromolecules* **2001**, 34, 1864-1872.
73. Cho, K.S.; Park, G.W. Fixed-point iteration for relaxation spectrum from dynamic mechanical data. *J. Rheol.* **2013**, 57, 647-678.

74. Bae, J.-E.; Cho, K.S. Logarithmic method for continuous relaxation spectrum and comparison with previous methods. *J. Rheol.* **2015**, *59*, 1081-1112.
75. Gramespacher, H.; Meissner, J. Interfacial tension between polymer melts measured by shear oscillations of their blends. *J. Rheol.* **1992**, *36*, 1127-1141.
76. Lee, J.B.; Lee, Y.K.; Choi, G.D.; Na, S.W.; Park, T.S.; Kim, W.N. Compatibilizing effect for improving mechanical properties of biodegradable poly (lactic acid) and polycarbonate blends. *Polym. Degrad. Stab.* **2011**, *96*, 553-560.
77. Puyvelde, P.V.; Velankar, S.; Moldenaers, P. Rheology and morphology of compatibilized polymer blends. *Curr. Opin. Colloid Interface Sci.* **2001**, *6*, 457-463.
78. Morrison, F.A. *Understanding rheology*. New York: Oxford University; **2001**.
79. Wagener, R.; Reisinger, T.J.G. A rheological method to compare the degree of exfoliation of nanocomposites. *Polymer* **2003**, *44*, 7513-7518.
80. Zhao, J.; Morgan, A.B.; Harris, D. Rheological characterization of polystyrene-clay nanocomposites to compare the degree of exfoliation and dispersion. *Polymer* **2005**, *46*, 8641-8660.
81. Wu, S. Phase structure and adhesion in polymer blends: A criterion for rubber toughening. *Polymer* **1985**, *26*, 1855-1863.

82. Jiang, W.; Yu, D.; Jiang, B. Brittle-ductile transition of particle toughened polymers: influence of the matrix properties. *Polymer* **2004**, 45, 6427-6430.
83. Maani, A.; Blais, B.; Heuzey, M-C.; Carreau, P.J.; Rheological and morphological properties of reactively compatibilized thermoplastic olefin (TPO) blends. *J. Rheol.* **2012**, 56, 625-647.